

An Earthquake Ground-Motion Model for Southwest Iberia

Amir Taherian^{*1}, Vitor Silva², Petros Kalakonas³, and Romeu Vicente¹

ABSTRACT

Ground-motion models (GMMs) are fundamental for the estimation of ground shaking for probabilistic seismic hazard assessment. Because of the paucity of ground motion recordings in regions of low seismicity, stochastic approaches are often employed to generate synthetic data. In this study, we developed a GMM using a stochastic simulation approach for southwest Iberia—a zone for which seismic hazard is usually assessed using models developed for other regions. We collected geological, tectonic, and ground-motion data for offshore and inland Iberia, and calibrated several parameters for a stochastic simulation. The resulting synthetic response spectra were used to train a machine learning algorithm (artificial neural network) capable of predicting peak ground acceleration, peak ground velocity, and spectral acceleration on rock ($V_{S30} = 760 \text{ m/s}$), along with the associated between-event and within-event terms. The resulting model was compared against other existing models for stable continental regions and ground-motion recordings for Portugal and Spain. The results indicate a good agreement with observations and the model can be used directly in probabilistic seismic hazard analysis for southwest Iberia.

KEY POINTS

- This study addresses the prediction of ground shaking intensities in southwest Iberia using a new ground-motion model (GMM).
- Offshore earthquakes require significantly higher stress drops to match observed ground-motion values.
- The findings suggest the need for further study and enhanced seismic monitoring of earthquakes in the region.

INTRODUCTION

A ground-motion model (GMM) is fundamental for the assessment of seismic hazard and risk for a given region. These models identify the distribution of earthquake intensity at different sites as a function of earthquake magnitude, source-to-site distance, and soil conditions. For regions defined as active shallow crustal (ASCR) or subduction tectonic zones (e.g., [Delavaud et al., 2012](#)), there are dozens of empirical models due to the abundance of ground-motion data (e.g., [Ambraseys et al., 2005](#); [Akkar and Bommer, 2010](#); [Zafarani et al., 2018](#)). For regions classified as stable continental regions (SCR) such as western Iberia, the seismic activity is considerably lower, and the paucity of ground-motion recordings hinders the development of empirical models in the same manner. In the 1980s, methods based on stochastic simulations (e.g., [Boore, 1983, 2003](#)) were proposed to generate synthetic ground-motion records compatible with these regions to overcome the scarcity of SCR data.

The current study aims at developing a stochastic-based GMM for western Iberia. The study area comprises mainland and offshore Portugal and southwest of Spain. This region is located near the Azores–Gibraltar plate boundary, separating the Eurasian and African plates. Despite the relatively low seismicity, this region has generated large-magnitude events such as the 1755 $M_w \sim 8.5$ Lisbon earthquake or the 1969 $M_w 7.8$ Algarve earthquake ([Vilanova et al., 2012](#)). This region has been classified as SCR in various studies, and typically GMMs for this tectonic regime lead to better predictions of ground shaking, in comparison with models developed for ASCR (e.g., [Boore and Atkinson, 2008](#); [Chiou and Youngs, 2008](#); [Akkar and Bommer, 2010](#)). Because of the lack of specific GMMs, the models developed for other SCRs (e.g., [Atkinson and Boore, 2006](#), for eastern North America [ENA]) have been used in seismic hazard and risk assessment studies. [Vilanova et al. \(2012\)](#) investigated the performance of GMMs developed for ASCRs and SCRs for the prediction of spectral acceleration (SA) using recorded offshore earthquakes in Portugal (e.g., 12 February 2007 $M_w 6.0$ earthquake), and concluded that GMMs for ENA tend to perform relatively well.

1. RISCO/University of Aveiro, Aveiro, Portugal,  <https://orcid.org/0000-0002-7012-3319> (AT);  <https://orcid.org/0000-0002-5456-1642> (RV); 2. Global Earthquake Model Foundation (GEM), Pavia, Italy; 3. Zurich Insurance Group, Zurich, Switzerland,  <https://orcid.org/0000-0002-2868-2328> (PK)

*Corresponding author: ar.taherian@ua.pt

Cite this article as Taherian, A., V. Silva, P. Kalakonas, and R. Vicente (2024). An Earthquake Ground-Motion Model for Southwest Iberia, *Bull. Seismol. Soc. Am.* **XX**, 1–26, doi: [10.1785/0120230250](https://doi.org/10.1785/0120230250)

© Seismological Society of America

Seismic hazard studies for this region use the same set of GMMs (mostly from ENA) for both inland and offshore Iberia. However, the findings from Diaz *et al.* (2016) showed that the crustal thickness in inland and offshore Iberia is in the ranges of 10–15 km and 25–35 km, respectively, which are considerably lower than the 50 km crustal thickness reported in ENA. These results might explain the low attenuation of seismic waves in Iberia described in Sousa and Oliveira (1996) and Vilanova *et al.* (2012). Furthermore, a recent study by Vales *et al.* (2020) investigated the anelastic attenuation for western Iberia using the Portuguese and Spanish ground-motion database and proposed Q-values at $f = 1$ Hz from 80 to 200, which is much lower than what has been reported for ENA. These two important studies highlight the need to explore a specific GMM for the region.

Based on the aforementioned findings, we divide the study region into two areas: inland and offshore. All ground-motion records from the Portuguese and Spanish seismic network databases (Instituto Português do Mar e da Atmosfera [IPMA] and Instituto Geográfico Nacional [IGN]) are collected and used to calibrate the modeling parameters for the stochastic simulations. This process leads to two sets of modeling parameters (i.e., inland and offshore) with the associated aleatory variability. Then, ground-motion simulations are performed to estimate the SA values on rock ($V_{S30} = 760$ m/s) for a large number of hypothetical earthquake scenarios for the region. These synthetic records are used to train, verify, and test an artificial neural network (ANN), capable of predicting ground shaking in the region with a high level of accuracy. The results of the calibrated model are compared with existing GMMs developed for other SCRs, as well as with recordings from past earthquakes in the region.

SEISMICITY AND SEISMIC HAZARD IN SOUTHWEST IBERIA

Iberia is in the southwest of the Eurasian plate, near the collision with the African plate. This tectonic environment has generated some of the highest offshore magnitude events in Europe, including the 1755 $M_w \sim 8.5$ Great Lisbon, the 1858 $M_w \sim 7.1$ Setubal, and the 1969 $M_w 7.8$ Algarve earthquakes (e.g., Vilanova and Fonseca, 2007; Buorn *et al.*, 2020). Destructive inland events have also occurred in the past, such as the 1531 $M_w \sim 6.9$ Lisbon, the 1909 $M_w 6.0$ Benavente, the 1954 $M_w 5.0$ Albolote, and the recent 2011 $M_w 5.1$ Lorca earthquakes (Fonseca and Vilanova, 2010). Significant events have also occurred in the Azores archipelago due to its location at the triple junction where the North American, Eurasian, and African plates meet, but this region has been excluded from the scope of this study. All these events caused significant damage in the respective regions, and, in particular, the 1755 Lisbon earthquake heavily damaged or destroyed more than 50% of the building stock and ~10% of the population around Lisbon perished (e.g., Oliveira *et al.*, 1988). According to the

recent unified declustered earthquake catalog for Europe (Danciu *et al.*, 2021), the majority of the inland events occur at relatively shallow depths (<15 km), whereas both shallow and deeper (>25 km) events are common in the offshore zone, along the Eurasian and African boundaries. Figure 1 presents the historical and instrumental earthquake catalog for the region covered by this study.

Most of the probabilistic seismic hazard models that cover this region indicate a peak ground acceleration (PGA) for the 475-year return period on rock ($V_{S30} = 760$ m/s) between 0.15g and 0.20g (Vilanova and Fonseca, 2007; Woessner *et al.*, 2015; Danciu *et al.*, 2021). However, some of these studies used GMMs developed for ENA or active shallow regions, which could lead to an underestimation of the seismic hazard, as later discussed in this study.

GENERATION OF SYNTHETIC RECORDS USING EXSIM

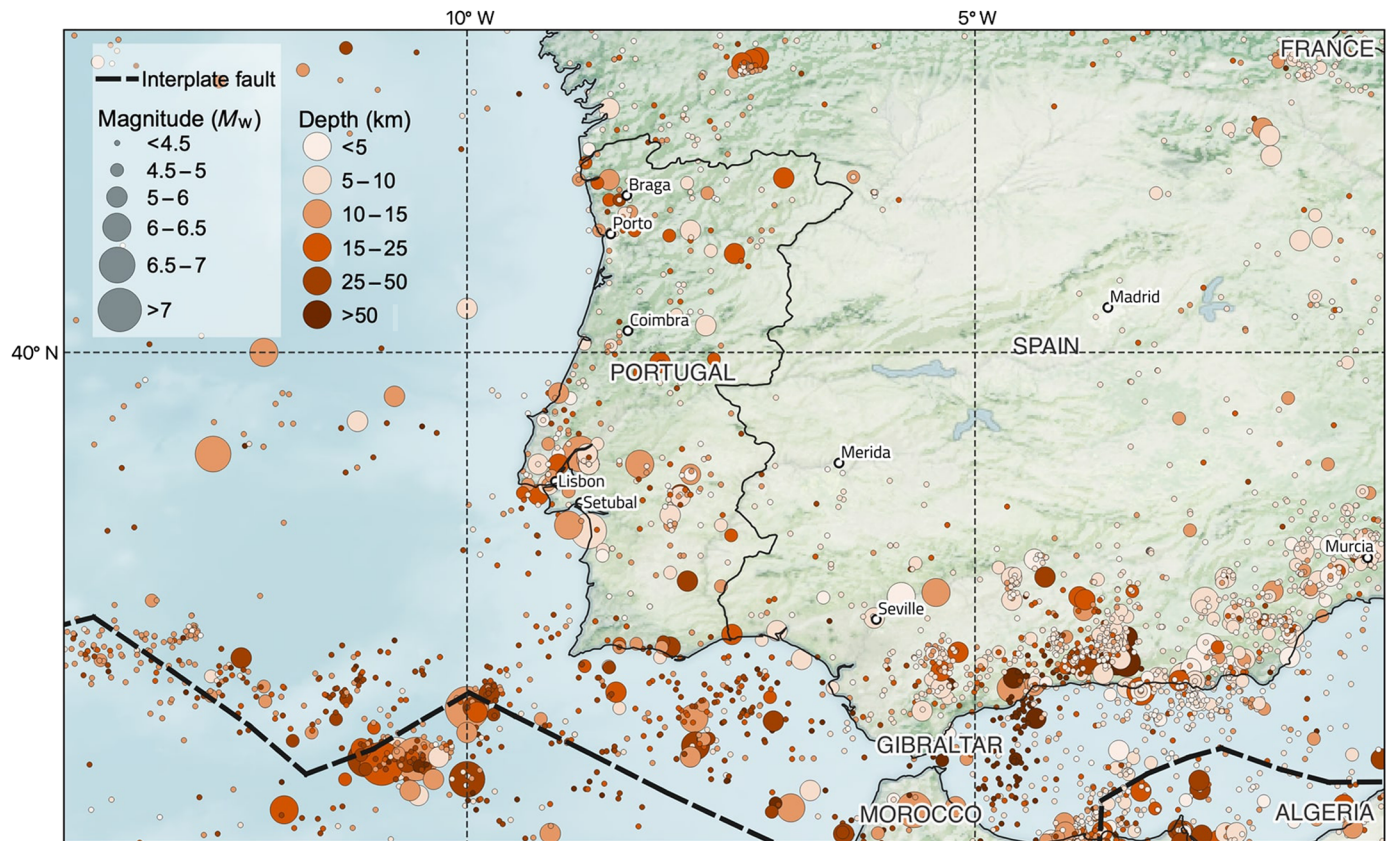
Methodology

The basis of the well-known stochastic approach for the simulation of earthquake ground-motion records was first proposed by Boore (1983). During the past decades, this method has been employed for the development of several GMMs for SCRs in different parts of the world such as ENA (Atkinson and Boore, 1995, 2006), the United Kingdom (Rietbroek *et al.*, 2013), Switzerland (Edwards and Fäh, 2013), Saudi Arabia (Sokolov *et al.*, 2021), and Australia (Allen, 2012).

This approach follows Brune's model for the calculation of Fourier amplitude spectra of shear waves radiated from the earthquake source, based on its seismic moment and stress (Brune, 1970, 1971). Based on the predicted source spectrum, the Fourier amplitude of different frequencies can be computed at each site using an attenuation and site function. Through equation (1), the Fourier amplitude of ground motion (A) is calculated as a function of frequency f , distance R (in kilometers), and seismic moment M_0 (in Newton meters) of the earthquake event:

$$A(M_0, R, f) = \left(\frac{CM_0 4\pi^2 f^2}{1 + (\frac{f}{f_0})^2} \right) \left(\frac{\exp[-\frac{\pi f R}{Q(f)\beta}]}{Z(R)} \right) \exp(-\pi\kappa_0 f), \quad (1)$$

in which f_0 is the corner frequency given by $4.9 \times 10^6 \beta (\frac{\Delta\sigma}{M_0})^{1/3}$; $\Delta\sigma$ represents the stress drop (in bars); and β is the crustal shear-wave velocity (in kilometer per second). The constant C can be computed as $\Re_{\theta\phi} FV / (4\pi\beta^3)$, in which $\Re_{\theta\phi}$ is the radiation pattern (equal to 0.55 for shear waves); F is the free-surface amplification (assumed as 2.0); V can be used to partition the ground onto two horizontal components (0.71); ρ represents the density of the crust; and R stands for the hypocentral distance (Boore, 2003). In the second term of the equation, $Z(R)$ is the geometrical spreading function, which is proportional to R^n . The coefficient n is usually assumed as



1 near the source and decreases with distance according to the Moho depth in the region. The frequency-dependent quality factor $Q(f)$ is an inverse measure of anelastic attenuation, which depends on the region. κ_0 is the diminution factor, which is typically accepted as a site parameter that describes the decay of spectral amplitude at high frequencies (Anderson and Hough, 1984; Haendel *et al.*, 2023). Because one of the goals of this study is to simulate large-magnitude offshore earthquakes in southwest Iberia, we employed a stochastic finite-fault methodology, allowing us to take into account important finite-fault features such as the geometry of larger ruptures and its effects on the predictions. To this end, large seismic faults are divided into several subsources, and each subsource is considered a small point source (Hartzell, 1978; Atkinson and Boore, 2006). The size of each subsource varies depending on the earthquake magnitude. The maximum length was 15 km for events with $M_w > 8.0$. The ground motions corresponding to each subsource are calculated by the stochastic point-source method as explained earlier. Then, contributions from each subsource are normalized, delayed, and summed in the time domain.

The extended finite-fault ground-motion simulation algorithm (EXSIM) code (Motazedian and Atkinson, 2005; Assatourians and Atkinson, 2007) is used to generate synthetic ground-motion records for a large suite of earthquake scenarios. EXSIM is a FORTRAN code that uses the stochastic finite-fault approach. To simulate the impact of finite-fault geometry

Figure 1. Instrumental and historical earthquake catalog for southwest Iberia (Danciu *et al.*, 2021). The color version of this figure is available only in the electronic edition.

on the frequency content of radiated ground motions more accurately, EXSIM employs the concept of dynamic corner frequency, which decreases over time as the rupture propagates. The term “dynamic corner frequency” implies that the frequency content of the seismic waves decreases over time during the earthquake rupture process. By accounting for this dynamic change in frequency content, the simulation aims to better represent the actual ground shaking observed during earthquakes (Motazedian and Atkinson, 2005). In this section, we describe the steps that were followed to collect existing ground-motion data and calibrate the modeling parameters for the simulations.

Data collection and processing

Despite the large historical events described previously, the ground-motion data for this region covers only events with the maximum moment magnitude of 6.0. In the case of Portugal, since the 1970s, IPMA has been responsible for monitoring the seismic activity in the Portuguese territory, which covers the extensive Azores–Gibraltar plate boundary segment (Carrilho *et al.*, 2021). Currently, 72 strong-motion stations are

operated in Portugal: 4 in the Madeira Islands, 28 in the Azores, and 40 in the mainland (Carrilho *et al.*, 2021). In the case of the Spanish territory, since 1977 the monitoring of seismic activity has been managed by IGN. Using 132 stations, this seismic network collects ground-motion data throughout the Iberian peninsula, Balearics, and the Canary Islands (Amaro-Mellado *et al.*, 2021). In this study, we use these databases to extract ground-motion records for events

with a minimum magnitude (M_w) of 3.0 within the geographical area with longitude 16° W to 1° E and latitude 36° to 42° N. In total, ground motion data from about 500 events were collected. We used the empirical magnitude conversion relationships developed by Di Giacomo *et al.* (2015) to convert all the magnitudes to M_w . We denote all converted M_w simply as M_w . Table 1 presents the most relevant earthquakes (with $M_w > 4.5$) used for the calibration of the modeling parameters.

TABLE 1
Major Seismic Events Used for Inversion of Stochastic Parameters

Event ID	Origin Time (yyyy/mm/dd hh:mm:ss)	M_w	Latitude	Longitude	Depth	Region
1	2008/01/11 00:21:45	4.7	36.48	-9.94	17	Southwest do C.S.Vicente
2	2009/12/17 01:37:51	6	36.49	-9.99	31	Southwest Cabo S.Vicente
3	2018/01/15 11:51:40	4.9	38.79	-7.93	11	Northeast Arraiolos
4	2018/09/04 06:12:58	4.6	40.2	-10.39	10	Abissal IbÁrica
5	2007/02/12 10:35:26	5.9	35.93	-10.49	37	Mar de Marrocos
6	2000/07/26 14:00:19	4.5	36.68	-2.98	1	Strait of Gibraltar
7	2000/10/27 12:35:54	4.5	35.03	-5.47	30	Strait of Gibraltar
8	2001/01/31 03:33:19	4.5	35.97	-1.15	13	Northern Algeria
9	2001/03/03 17:10:49	4.6	37.35	-5.32	2	Spain
10	2001/09/19 01:25:43	4.8	37.18	-2.24	1	Spain
11	2002/02/04 20:09:29	4.9	37.17	-2.67	11	Spain
12	2002/02/05 12:41:16	4.9	37.14	-2.67	5	Spain
13	2002/02/20 16:19:38	4.6	36.87	-6.26	21	Strait of Gibraltar
14	2002/08/06 06:16:19	4.7	38.1	-2	10	Spain
15	2002/08/06 22:54:31	4.7	37.94	-1.88	7	Spain
16	2002/08/07 10:55:07	4.6	36.15	-0.47	30	Western Mediterranean Sea
17	2003/02/18 13:09:36	4.7	35.89	-3.52	8	Strait of Gibraltar
18	2003/02/24 00:44:51	4.5	36.8	-6.99	31	Strait of Gibraltar
19	2003/06/20 14:43:49	4.5	38.14	-0.68	1	Spain
20	2003/11/16 21:36:11	4.5	37.69	-2.79	12	Spain
21	2004/02/24 02:27:46	6.3	35.26	-4	9	Strait of Gibraltar
22	2004/02/24 02:31:17	4.5	35.14	-3.98	17	Strait of Gibraltar
23	2004/02/24 02:32:18	4.7	35.19	-3.94	1	Strait of Gibraltar
24	2004/02/24 02:33:52	4.8	35.58	-2.16	1	Strait of Gibraltar
25	2004/02/24 02:36:38	4.6	35.17	-3.96	22	Strait of Gibraltar
26	2004/02/24 04:40:31	5.4	35.17	-3.98	9	Strait of Gibraltar
27	2004/02/24 06:20:16	4.5	35.22	-4.06	11	Strait of Gibraltar
28	2004/02/24 18:53:02	4.8	35.15	-3.97	22	Strait of Gibraltar
29	2004/02/25 05:21:13	4.5	35.21	-4.07	10	Strait of Gibraltar
30	2004/02/25 12:44:56	5.2	35.32	-4.08	10	Strait of Gibraltar
31	2004/02/26 12:07:03	4.9	35.27	-4.12	21	Strait of Gibraltar
32	2004/03/02 20:36:25	4.5	35.31	-4.01	1	Strait of Gibraltar
33	2004/03/03 01:45:24	4.5	35.41	-4.08	15	Strait of Gibraltar
34	2004/03/07 06:37:52	5.1	35.18	-4.09	11	Strait of Gibraltar
35	2004/03/12 17:21:49	4.7	35.04	-4.15	1	Strait of Gibraltar
36	2004/03/15 22:18:31	4.5	35.42	-4.07	0	Strait of Gibraltar
37	2004/08/14 01:55:44	4.5	35.23	-3.91	10	Strait of Gibraltar
38	2004/10/10 08:13:55	4.5	35.03	-4.14	1	Strait of Gibraltar
39	2004/12/02 17:50:43	4.9	35.09	-3.03	14	Strait of Gibraltar
40	2004/12/04 10:30:01	5.1	35.18	-3.07	25	Strait of Gibraltar
41	2004/12/04 15:42:10	4.6	35.14	-3.05	20	Strait of Gibraltar
42	2005/04/17 22:58:47	4.5	39.41	-0.02	10	Spain
43	2005/05/25 00:48:46	4.8	37.24	-4.96	4	Spain
44	2005/06/30 01:19:20	4.6	36.79	-1.67	10	Western Mediterranean Sea
45	2007/05/18 13:05:40	4.6	35.36	-6.25	48	Strait of Gibraltar

(Continued)

TABLE 1 (Continued)

Event ID	Origin Time (yyyy/mm/dd hh:mm:ss)	M_w	Latitude	Longitude	Depth	Region
46	2007/06/30 03:53:45	4.5	37.11	-5.37	11	Spain
47	2007/09/08 16:41:30	4.8	35.82	-3.52	5	Strait of Gibraltar
48	2008/01/09 22:24:03	4.6	35.62	-0.58	10	Northern Algeria
49	2008/06/06 20:02:58	5.5	35.92	-0.61	10	Northern Algeria
50	2008/10/02 04:02:52	4.7	37.11	-5.39	7	Spain
51	2008/10/21 05:55:45	4.5	36.47	-2.7	6	Strait of Gibraltar
52	2009/05/25 09:18:38	4.7	35.57	-6.94	10	Strait of Gibraltar
53	2010/04/22 01:23:59	4.8	35.33	-6.25	42	Strait of Gibraltar
54	2010/05/28 11:31:20	5	38.65	-4.13	1	Spain
55	2010/08/25 08:29:02	4.5	36.39	-6.07	12	Strait of Gibraltar
56	2011/05/11 15:05:12	4.5	37.73	-1.71	5	Spain
57	2011/05/11 16:47:25	5.1	37.65	-1.69	7	Spain
58	2013/12/16 07:06:21	4.8	35.56	-6.98	45	Strait of Gibraltar
59	2013/12/29 21:46:19	4.5	36.82	-4.12	35	Strait of Gibraltar
60	2014/08/19 13:38:23	4.6	36.93	-5.56	11	Strait of Gibraltar
61	2015/02/23 16:16:29	5	39.1	-2.61	11	Spain

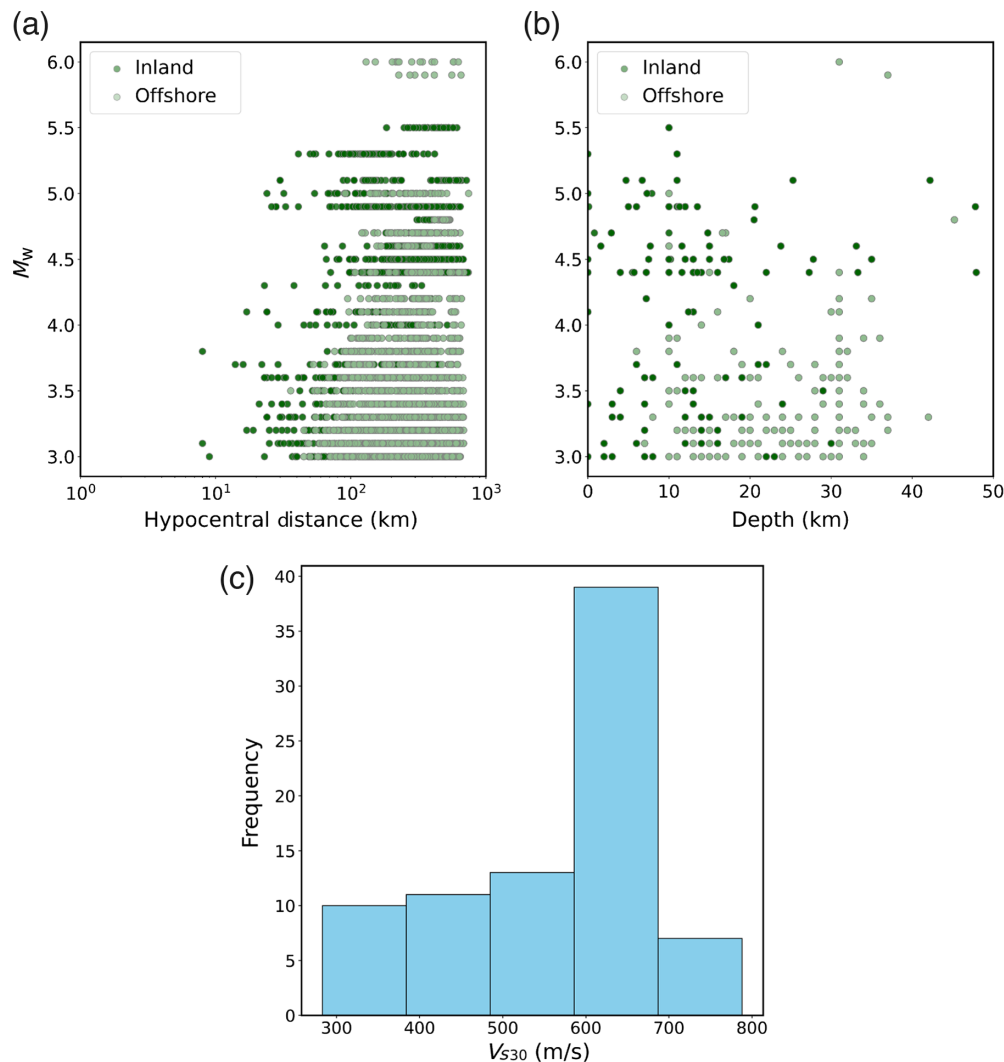


Figure 2. (a) Distribution of magnitude (M_w) versus hypocentral distance (R), (b) magnitude (M_w) versus depth for the compiled earthquake catalog, and (c) histogram of the V_{S30} of the seismic stations considered in this study. The color version of this figure is available only in the electronic edition.

For the processing of ground-motion data, the recordings had to be corrected for the instrument response by applying appropriate filters using the open library ObsPy (Beyreuther *et al.*, 2010). The signal-to-noise ratio (SNR) was computed for each signal by comparing the spectral amplitudes of both the recorded signal (signal + noise) and the pre-event signal (noise). We used a criterion of SNR greater than 3 to exclude noise from the actual recording. The duration of the time window used for noise analysis was set to 20 s before the arrival of the P waves. Figure 2 illustrates the distribution of magnitude (M_w), hypocentral distance (R), and depth of the resulting set of ground-motion records along with the distribution of the V_{S30} of the recording stations. The V_{S30} values for each seismic station were estimated and provided by IPMA and IGN. Despite the coverage of these seismic networks, the recorded data from past major earthquakes is relatively scarce and only

covers low-to-moderate magnitude earthquakes. Although the range of V_{S30} of the recording stations is from 280 to 800 m/s, for the inversion of stochastic parameters, we only considered data from stations with a minimum V_{S30} of 600 m/s. An exception was made for the determination of the stress parameter, given that the vertical component of ground motions on soil sites is less affected by site effects (Allen, 2012). In total, we have used 12,230 records from 494 seismic events. Out of the total dataset, 6550 records were sourced from sites where the V_{S30} exceeds 600 m/s.

Input parameters for stochastic simulations

The most relevant parameters for predicting Fourier amplitude as a function of magnitude and distance (as described in equation 1) are the stress drop ($\Delta\sigma$), attenuation parameters (Z and Q), and diminution factor (κ_0). In this section, we describe how each parameter has been calibrated for our region of interest using the locally recorded ground motion data. We followed closely the procedure demonstrated for other SCRs such as Switzerland (Edwards and Fäh, 2013) and Australia (Allen, 2012), where the number of recordings is also limited.

Attenuation parameters. The attenuation was defined using the geometrical spreading parameter (Z) and the anelastic attenuation (Q). The geometrical spreading represents the attenuation of shear waves with distance, which is governed by the regional crustal structure, and it can be assumed to be proportional to R^n . Previous studies have shown that the slope of the geometrical spreading curve (i.e., value of n) is strongly affected by the distance due to discontinuities in the earth's crust (Atkinson and Mereu, 1992; Lam *et al.*, 2000). We performed a regression analysis to define a geometrical spreading function for the region. Given the lack of records in different ranges of magnitudes, we followed the proposal from Atkinson (2004) to normalize the Fourier amplitude spectra for the regression analysis, as such results can be used directly regardless of the magnitude of each record. Following the recommendation of Atkinson (2004) and Allen (2012), which stated that for frequencies $f \leq 2$ Hz the effects of anelastic attenuation are negligible at distances below 100 km, we use Fourier displacement spectra at 2 Hz for the calibration of the geometrical spreading. We assume that the source spectra for each earthquake can be estimated by averaging the product of the Fourier amplitude by its distance (R). For this purpose, only records with a distance below 100 km were used. Moreover, only earthquakes with at least three records in this range of distance are considered in the analyses. We normalize the Fourier spectrum of each record assuming $\log FAS = 0$ at $R = 1$ km. We calculate the normalized spectral amplitudes at 2 Hz using the equation (2):

$$\log A_{ij} = \log A_{ij}(f) - (1/N) \sum_{i=1}^N [\log A_{ij}(f) + \log R_{ij}], \quad (2)$$

in which A_{ij} is the normalized amplitude for earthquake i at station j ; A_{ij} is the recorded amplitude of earthquake i at hypocentral distance R_{ij} ; and the sum is over the number (N) of stations that recorded earthquake i .

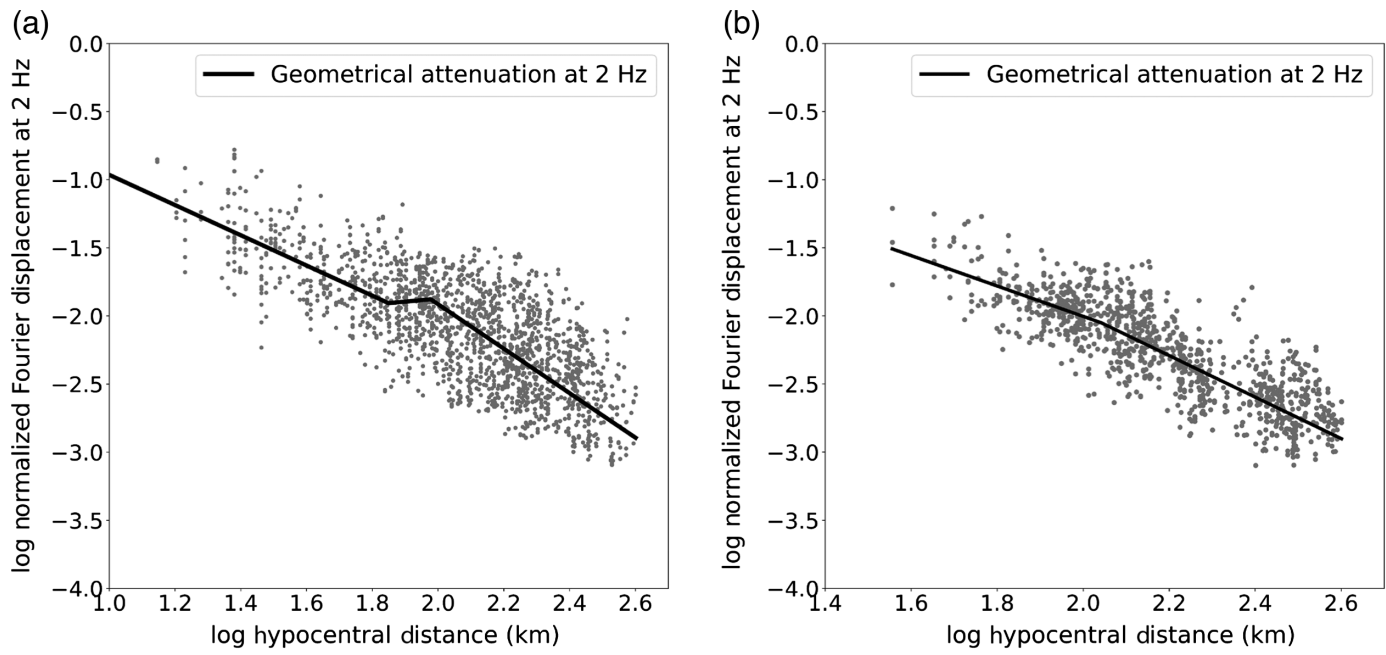
A preliminary analysis of the normalized Fourier amplitude data showed that the slope of the attenuation curve varies significantly between the inland and offshore regions. Therefore, considering these results and the findings of Diaz *et al.* (2016) on the variation of crustal thickness between inland and offshore Iberia, a decision was made to divide the model between inland and offshore. We use the Python piecewise-regression package (Pilgrim, 2021) and the method proposed by Muggeo (2003), in which the breakpoint positions and the straight-line models are simultaneously fit using an iterative method. The best-fit model is defined for the case in which the standard deviation of the residuals is minimal. For the inland model, a three linear piecewise model was defined as described by equation (3), in which the low-frequency Fourier amplitude attenuates as $R^{-1.1}$ for distances below 70 km. For distances between 70 and 100 km, there is a slight amplification of amplitudes equal to $R^{0.2}$, and for distances above 100 km, the low-frequency seismic waves attenuate more rapidly ($R^{-1.55}$):

$$\log Z(R_{ij}) = \begin{cases} 1.1 \log R_{ij} & R_{ij} \leq 70 \\ 1.1 \log(70) - 0.2 \log\left(\frac{R_{ij}}{70}\right) & 70 < R_{ij} < 100 \\ 1.1 \log(70) - 0.2 \log\left(\frac{100}{70}\right) + 1.55 \log\left(\frac{R_{ij}}{100}\right) & R_{ij} \geq 100 \end{cases}. \quad (3)$$

For the offshore model, a bilinear model was defined as described by equation (4), in which the Fourier amplitude attenuates as $R^{-1.1}$ for distances below 115 km, and more rapidly ($R^{-1.5}$) for distances above 115 km. Figure 3 depicts the geometrical spreading curve derived for inland and offshore southwest Iberia:

$$\log Z(R_{ij}) = \begin{cases} 1.1 \log R_{ij} & R_{ij} \leq 115 \\ 1.1 \log(115) + 1.5 \log\left(\frac{R_{ij}}{115}\right) & R_{ij} > 115 \end{cases}. \quad (4)$$

As previously discussed, the second source of attenuation of seismic waves is anelastic attenuation, which is represented by the quality factor (Q). The quality factor (Q) quantifies the amount of energy loss or attenuation experienced by seismic waves because they propagate through a medium. A higher (Q) value means that seismic waves lose less energy because they travel through the medium, resulting in lower attenuation. Conversely, a lower (Q) value indicates higher attenuation, meaning that seismic waves lose more energy and decay



more rapidly as they propagate (Wilkie and Gibson, 1995; Allen, 2012).

To define the quality factor, the natural logarithm of source normalized Fourier amplitude at each frequency must be corrected for geometrical spreading $Z(R_{ij})$ and related to the distance. This process is shown in Figure 4 for inland data at four frequencies. To estimate the frequency-dependent quality factor, $Q(f)$, at each frequency, a linear regression is performed against hypocentral distance. This regression analysis assumes that the reciprocal of the quality factor, Q^{-1} , is proportional to the natural logarithm of the corrected Fourier amplitude ($\ln(A_{g,ij})$) divided by the distance (R). The relationship can be expressed as: $Q^{-1} \propto \frac{\ln(A_{g,ij})}{R}$, in which $\ln(A_{g,ij})$ is the normalized Fourier displacement spectra corrected for geometrical spreading and estimated using equation (5):

$$\ln(A_{g,ij}) = \ln(A_{n,ij}) - \log Z(R_{ij}). \quad (5)$$

As presented in Figure 4, the effect of anelastic attenuation for low frequencies is

Figure 3. Geometrical attenuation curve derived using normalized Fourier amplitude spectrum at 2 Hz for (a) inland and (b) offshore events in southwest Iberia.

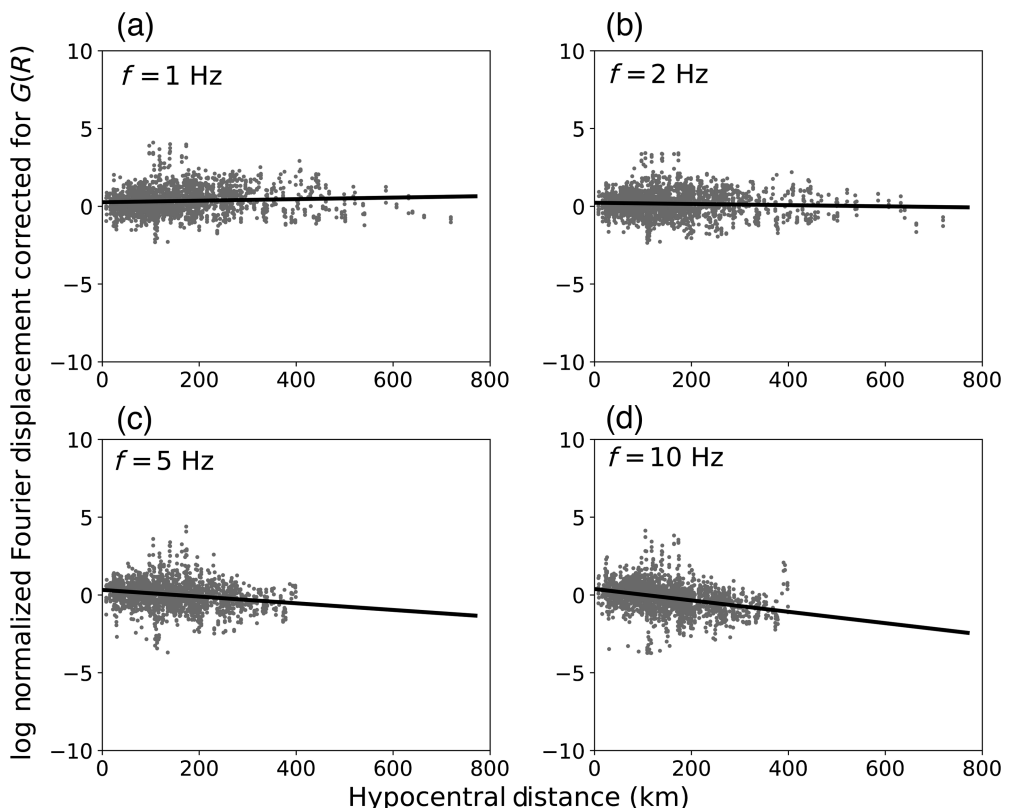
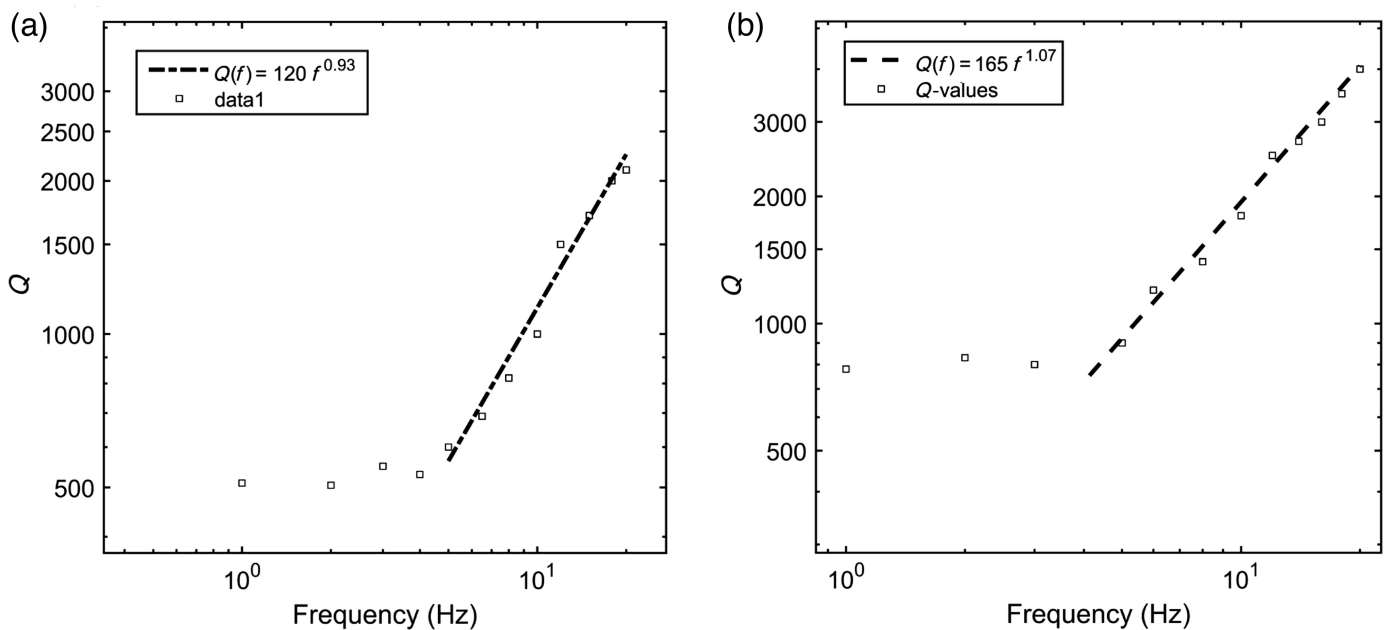


Figure 4. Natural logarithm of normalized spectra ($\ln A_{n,ij}$) corrected for $G(R)$ against R at four different frequencies. (a) 1 Hz, (b) 2 Hz, (c) 5 Hz, and (d) 10 Hz.



negligible. However, because the frequency increases, the effect of anelastic attenuation becomes more evident at larger distances. Following [Allen et al. \(2007\)](#), for frequencies of 5 Hz and greater, we excluded data that were recorded beyond 400 km.

It is important to note that in this context, this process aims to derive the frequency-dependent quality factor ($Q(f)$) rather than a single Q value. The frequency-dependent quality factor is modeled as: $Q(f) = Q_0 f^\gamma$, in which Q_0 is the quality factor at a referenced frequency, and γ is a frequency-dependent exponent. Figure 5 illustrates the estimated Q values against frequency using the inland and offshore data.

Equation (6) presents $Q(f)$ for inland and offshore ground motions. In both cases, Q has a minimum value near $f = 1$ Hz. The value of Q_{minimum} for inland and offshore is 500 and 800, respectively. This result is in agreement with previous studies that considered lower attenuation for offshore earthquakes in the region ([Carvalho et al., 2008](#); [Vales et al., 2020](#)). However, we note that the attenuation model presented here is based on limited data, especially for shorter distances. The employment of more advanced techniques for the inversion of the stochastic parameters is part of future studies, as further discussed in the concluding remarks:

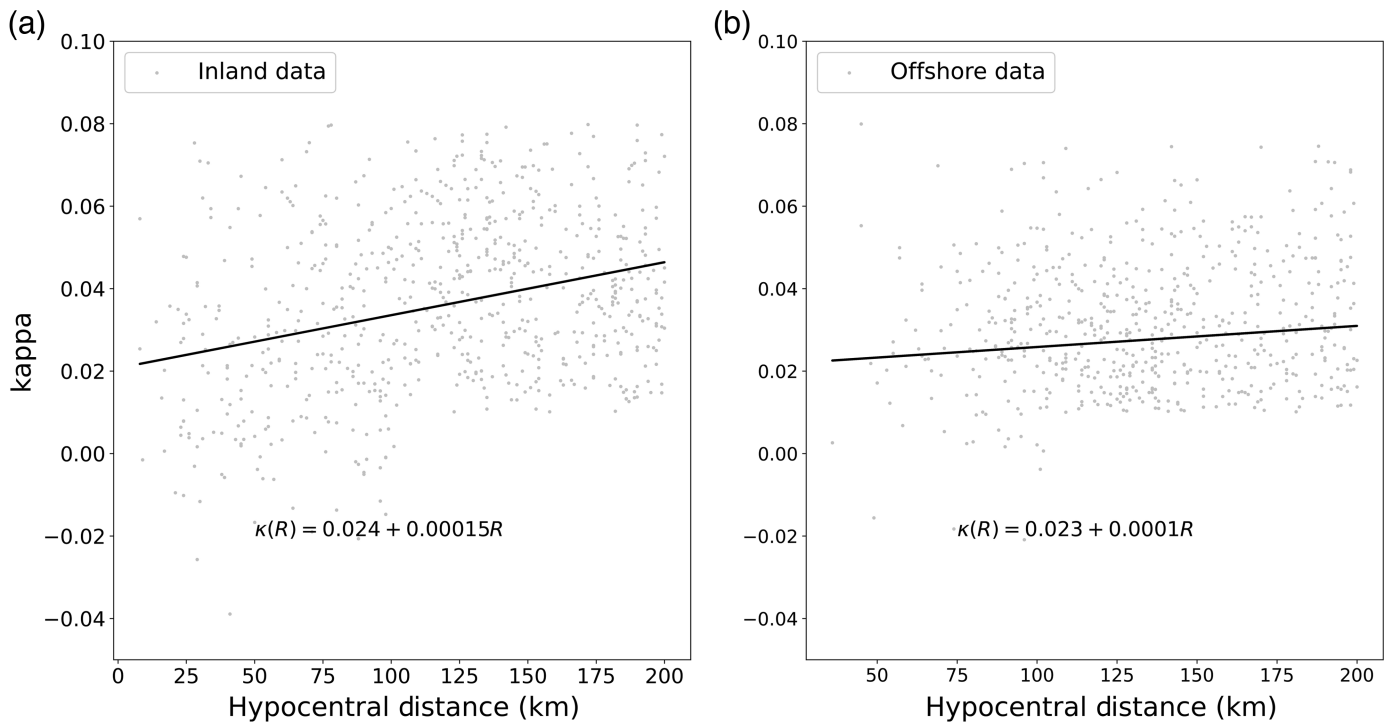
$$Q(f) = \begin{cases} 120f^{0.93} & \text{Inland} \\ 165f^{1.07} & \text{Offshore} \end{cases} \quad (6)$$

Spectral decay parameter. We modeled the shape of the amplitude of high-frequency signals using the spectral decay factor κ_0 , as recommended by [Anderson and Hough \(1984\)](#). Previous studies (e.g., [Van Houtte et al., 2011](#)) showed an inverse correlation between V_{S30} and the κ_0 parameter, but further investigations have identified an asymptotic trend of κ_0 at

Figure 5. Q -values determined from regression analysis using (a) inland, and (b) offshore data. The black dashed line shows the linear fit to the Q -values.

very high shear-wave velocities ([Xu et al., 2020](#); [Haendel et al., 2023](#)). Because in this study we aim at developing a GMM for rock sites ($V_{S30} = 760$ m/s), we consider only vertical-component records for stations with V_{S30} ranging from 600 to 800 m/s. We calculate the slope of the smoothed Fourier amplitude spectrum corrected for anelastic attenuation in the frequency range of 12–20 Hz. The κ values for the entire database range from -0.02 to 0.08. Figure 6 shows the linear regression of κ_0 values with distance for inland and offshore events. Using equation $\kappa_R = \kappa_0 + mR$, the near-source spectral decay parameter (κ_0) for both inland and offshore events was estimated at 0.025. From this regression analysis, we estimate a standard deviation of 0.015. This value is close to the κ_0 estimated by an empirical equation proposed by [Van Houtte et al. \(2011\)](#) assuming $V_{S30} = 760$ m/s.

Brune stress drop. The most challenging parameter required for the stochastic simulations is arguably the stress drop ($\Delta\sigma$). This parameter controls the amplitude of high-frequency signals radiated from the source. It is generally agreed that in SCR earthquakes with the same magnitude produce higher ground motions at higher frequencies (for PGA and SA at 2 Hz and above), in comparison with active shallow regions as a result of lower stress-drop values ([Frankel, 2004](#)). This is mostly because fault asperities in stable regions generally possess higher frictional strength than in active regions, thus requiring higher stress to overcome the rigidity of the rocks in the crust (e.g., [Scholz et al., 1986](#); [Allen, 2012](#)). Different methods for calibrating this parameter can be found in the



literature, ranging from simple formulae as suggested by Aki (1972) based on fault rupture area to more complex methods that rely on specific parameters derived from recorded events following Brune's model (Brune, 1970, 1971). The Brune stress parameter $\Delta\sigma$ is often termed stress drop, yet it is important to recognize its nature as a model-specific parameter rather than a fundamental theoretical attribute of the earthquake rupture. This distinction is crucial because different source models and methodologies may yield different estimates of stress drop for the same earthquake, depending on the assumptions and simplifications of each model (Atkinson and Beresnev, 1997).

Alternatively, it is also possible to perform trial simulations using different values of $\Delta\sigma$ to reproduce the Fourier acceleration of high-frequency signals calculated from records at certain distances (Atkinson and Boore, 2006). Considering the attenuation function and spectral decay parameter that were defined earlier in this study, we estimated the average source displacement spectra for each earthquake with at least three records. Then, we fitted the ω^{-2} source model to the average source spectra to find the best estimate of the corner frequency (f_c) for each earthquake (Brune, 1970, 1971). The source model is defined in equation (7):

$$A(M_0, f) = \frac{CM_0}{1 + \left(\frac{f}{f_c}\right)^2}. \quad (7)$$

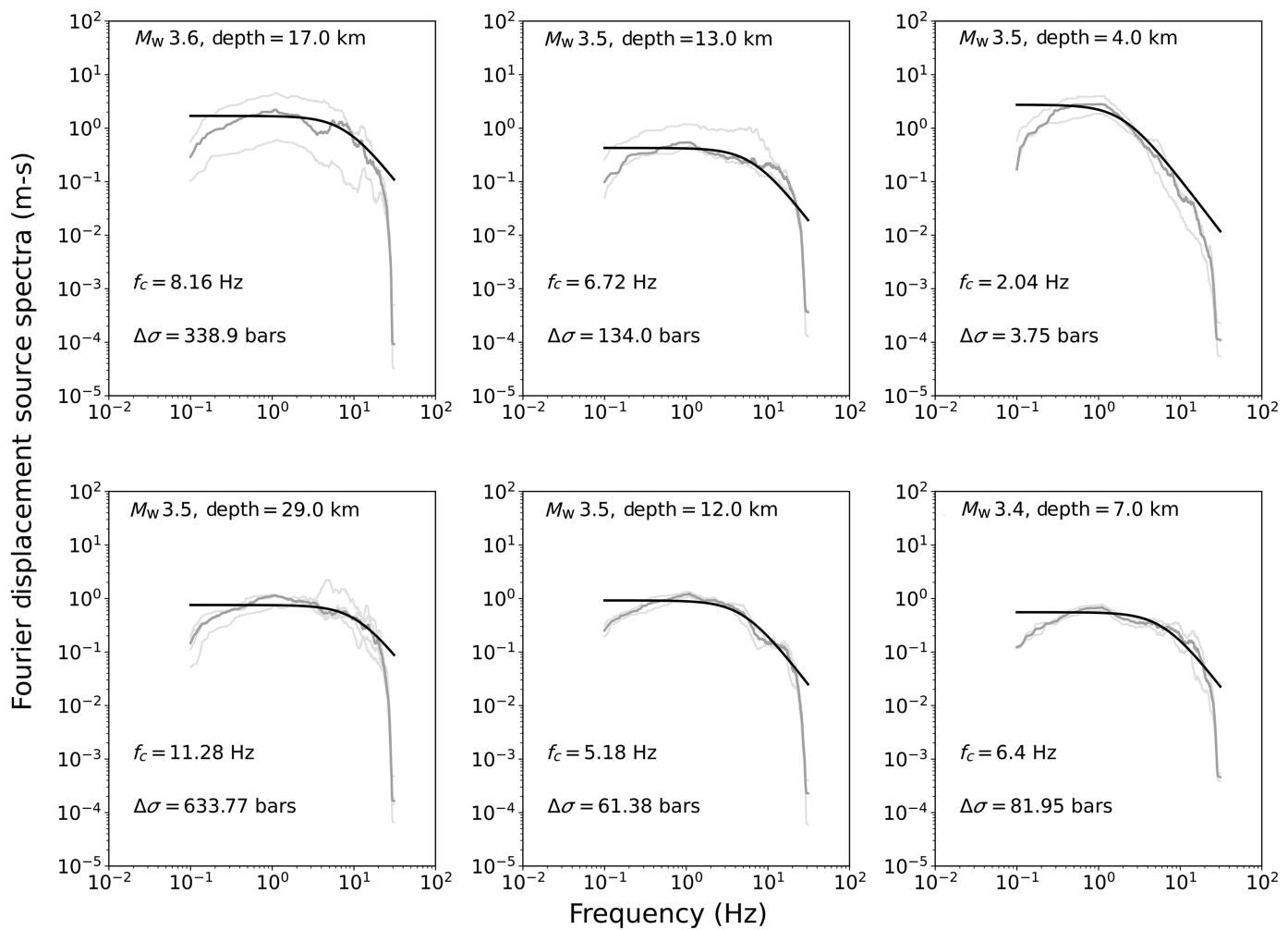
According to Brune's model, the stress drop is subsequently estimated using equation (8):

$$\Delta\sigma = \frac{7M_0}{16r^3}, \quad (8)$$

Figure 6. Illustration of the estimation of the κ_0 parameter for (a) inland and (b) offshore events.

in which $r = \frac{2.34\beta}{2\pi f_c}$ is the source radius of a circular fault (Brune, 1970, 1971). Figure 7 illustrates the calibration of stress drop for some events in the database. The results of these analyses indicate that the stress drop must be considerably larger for offshore events to fit the average source spectra, in comparison with inland events. The median stress values calculated for inland and offshore events are 50 and 140 bars, respectively. Our proposed values differ from the stress value of 50 bars suggested by Carvalho *et al.* (2008), which used the entire Portuguese ground-motion database. The main reason for this difference is that these authors assumed the same attenuation model for the entire region (inland and offshore), despite the differences in the crustal thickness between the two regions, as reported by Diaz *et al.* (2016).

Allmann and Shearer (2009), using their global database, studied the correlation of stress drop with fault mechanism. Their study showed that there is a clear dependence of stress drop on the faulting mechanism. The highest values are calculated for strike-slip earthquakes with a median of 100 bars, whereas for the reverse and normal earthquakes the median value is around 20–30 bars. In the current study, given the limited number of recordings for earthquakes with different fault mechanisms for Iberia, this separation of data was not possible. Some studies also investigated the magnitude dependence of stress drop; however, no strong correlation between these parameters has been reported (e.g., Allmann and Shearer, 2009; Dif *et al.*, 2020).



Duration of motion. The total duration of shaking (T) is composed of two components: source duration and path duration, as presented in equation (9):

$$T = T_0 + dR, \quad (9)$$

in which $T_0 = \frac{1}{f_c}$ is the source duration and d is a path-dependent coefficient. It is important to define the path-dependent parameter accurately because the overestimation of duration can lead to lower peak motions (Boore, 2003). Edwards and Fäh (2013) stated that it is common to define the observed duration of shaking as the time over which 5%–75% or 5%–95% of the cumulative square velocity or acceleration is encapsulated (e.g., Raoof *et al.*, 1999; Bay *et al.*, 2003, Kempton and Stewart, 2006). Drouet and Cotton (2015) in their stochastic model for the French Alps studied the effect of choosing acceleration or velocity for the development of a duration model and concluded that in both cases the results are very similar. In this study, the total duration is defined as the time window over which 5%–80% of the cumulative square velocity ($T_{v,(5\%-80\%)}$) is encapsulated (e.g., Allen, 2012). The goal is to estimate the value of the path-dependent coefficient (d) within different

Figure 7. Demonstration of the fitting of Brune's source spectrum to average Fourier source spectra and calibration of corner frequency and stress drop for selected events. The average source spectrum (gray thick line), superimposed on individual source-corrected spectra (gray thin lines), for several representative earthquakes. The theoretical Brune source spectrum is superimposed in each subplot (black thick line).

ranges of distance. For this purpose, velocity time histories for distances below 300 km were band-pass filtered and then used to compute $T_{v,(5\%-80\%)}$. Then, the source duration was subtracted from the total duration to calibrate the path-dependent parameter. Again, a piecewise linear regression analysis was performed for inland and offshore data separately. Figure 8 shows the regression of the observed path duration for both cases. A trilinear model was calibrated using inland data as described by equation (10), whereas the bilinear model expressed by equation (11) led to a better fitting for the offshore events:

$$d = \begin{cases} 0.13 & R \leq 70 \text{ km} \\ 0.09 & 70 \text{ km} < R \leq 120 \text{ km}, \\ 0.05 & R > 120 \text{ km} \end{cases} \quad (10)$$

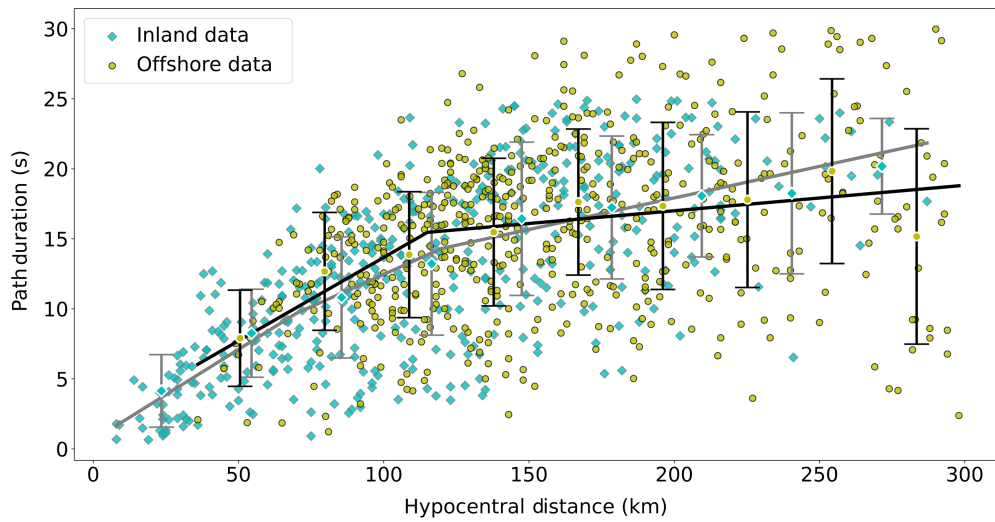


Figure 8. Observed path duration from inland and offshore earthquakes in southwest Iberia. The duration model was developed for the offshore model (black line) and inland model (gray line), and their corresponding error bars are indicated in this figure. The color version of this figure is available only in the electronic edition.

$$d = \begin{cases} 0.12 & R \leq 115 \text{ km} \\ 0.02 & R > 115 \text{ km} \end{cases} \quad (11)$$

Ground-motion simulations. Table 2 summarizes all the parameters that were used for the stochastic ground-motion simulations, along with the associated references.

As illustrated throughout this section, some of these parameters have a large aleatory variability, which must be propagated into the ground-motion simulations. We calculated

the variability in the geometrical spreading coefficient, stress drop, and spectral decay (κ_0) parameters, and assumed specific probabilistic distributions as described in Table 3. In the case of the attenuation model, the variability is captured through the geometrical spreading coefficient. For this purpose, a normal distribution is used considering the mean and standard deviation derived from the regression analysis described earlier in this study. Although we recognize that uncertainty in both attenuation parameters, for the sake of simplicity only the uncertainty in the geometrical spreading coef-

ficient was considered (e.g., Atkinson and Boore, 2006; Allen, 2012). This assumption is reasonable, given that the anelastic attenuation (Q) mostly affects ground motion at distances larger than 100 km (Atkinson, 2004), where we assumed a higher variability in the geometrical spreading parameters.

Similarly for the modeling of stress drop, we divided the estimated stress values into two main groups: inland and offshore. The mean and standard deviations are estimated and propagated during the stochastic simulations following a Monte Carlo approach. The median stress values in our simulations are 50 and 140 bars for the inland and offshore

TABLE 2
Median Input Parameters for Ground-Motion Simulation with Extended Finite-Fault Ground-Motion Simulation Algorithm (EXSIM)

Parameter	Median Value	Source
Crustal shear-wave velocity (β)	3.5 km/s	Vales et al. (2020)
Crustal density (ρ)	2.8 g/cm ³	Vales et al. (2020)
Stress drop ($\Delta\sigma$)	50 bars (inland), 140 bars (offshore)	This study
Rupture propagation speed	0.8 β	Assumed in this study
Kappa (κ_0)	0.025	This study
Geometrical spreading function, R^n , $n =$	Inland -1.1 ($R \leq 70$ km) 0.2 ($70 \text{ km} < R \leq 100$ km) -1.57 ($R > 100$ km) Offshore -1.1 ($R \leq 115$ km) -1.5 ($R > 115$ km)	This study
Quality factor (Q)	$Q(f) = \begin{cases} \text{Max}(500, 120f^{0.93}) & \text{Inland} \\ \text{Max}(800, 165f^{1.07}) & \text{Offshore} \end{cases}$	This study
Distance-dependent duration, $d(R, d) =$	Inland 0.13 ($R \leq 70$ km) 0.09 ($70 \text{ km} < R \leq 120$ km) 0.05 ($R > 120$ km) Offshore 0.12 ($R \leq 115$ km) 0.02 ($R > 115$ km)	This study
Hypocenter location and slip duration	Random	Assumed in this study
Pulsing percentage (%)	50	Assumed in this study
Fault geometry	Wells and Coppersmith (1994)	
Site conditions	Rock ($V_S = 760$ m/s)	Assumed in this study

TABLE 3
Aleatory Variability in Key Modeling Parameters

Parameter	Distribution Type	Mean	Standard Deviation
Stress drop	Lognormal	1.70 2.15	0.30 0.30
Kappa	Truncated normal	0.025 (0.01–0.05)	0.015
Geometrical spreading	Normal	Inland –1.1 ($R \leq 70$ km) 0.2 (70 km < $R \leq 100$ km) –1.55 ($R > 100$ km) Offshore –1.1 ($R \leq 115$ km) –1.5 ($R > 115$ km)	0.15 0.20 0.30 0.15 0.30
Depth	Truncated normal	10 km (2–30 km)	Inland: 13 km Offshore: 20 km

datasets, respectively. These values were derived from the stress-drop analysis previously presented. The logarithm of stress is assumed to follow a normal distribution, with a mean log stress of 1.70 and 2.15 for inland and offshore events, respectively, and a standard deviation of 0.30 log units for both cases. The logarithm of stress is considered normally distributed (e.g., Atkinson and Boore, 2006; Edwards and Fäh, 2013), with a mean log stress of 1.70 and 2.18 for inland and offshore, respectively, and a standard deviation of 0.30 log units for both cases. For the modeling of kappa parameter, a truncated normal distribution is assumed (e.g., Allen, 2012), with a mean value of 0.025 and a standard deviation of 0.015 for both inland and offshore cases.

For the sake of simplicity, we assumed the remaining variables as deterministic, as investigating the aleatory and epistemic uncertainty in these parameters is out of the scope of this study. To avoid unrealistic values for the spectral decay parameter (κ_0) and depth of the seismic events, we adopted truncated distributions.

The ground-motion simulations were performed using EXSIM, assuming the parameters listed in Tables 2 and 3. To perform ground-motion simulations on rock ($V_S = 760$ m/s), we used the generic site amplification factors proposed by Boore (2016). The uncertainty in the geometrical spreading, spectral decay (κ_0), and stress drop were sampled based on the event type (inland or offshore) using a Monte Carlo sampling process and considering the distributions presented in Table 3. For the inland scenarios, the ground motions were simulated considering hypothetical stations with distances (from the center of the top of the fault) ranging from 1 to 600 km and assuming azimuths from 0° to 180° . For the offshore events, to have a more realistic distribution of distances and azimuths, we sampled thousands of events using the recently released European Seismic Source Model (Danciu *et al.*, 2021) and assumed a hypothetical network of stations located inland on an evenly spaced grid of $10\text{ km} \times 10\text{ km}$. The number of trials for each simulation was 10. In total, more

than 1 million horizontal ground-motion records were generated for rock sites. The PGA, peak ground velocity (PGV), and 5% damped SA were computed for each record. These results were then used to train an ANN to predict ground motion, as discussed in the following section.

APPLICATION OF ANN TO PREDICT GROUND SHAKING

Different functional forms have been used in the last decades to predict ground shaking using empirical or synthetic ground-motion records (Douglas, 2022). In general, these expressions are composed of three components (i.e., event, path, and site terms) and two random variables (i.e. between and within-event aleatory variability) (e.g., Boore *et al.*, 2014). One of the advantages of such formulations is the fact that it allows extrapolating the predictive model to combinations of magnitude, source-to-site distance, and site conditions not necessarily well covered by the ground-motion data, as each term has a physical meaning. For the study presented herein, this advantage is less relevant, given that the stochastic simulation adopted herein allows generating records for all combinations of magnitude and distance. For this reason, we used the mixed-effects method (e.g., Stafford, 2014) to calibrate a machine learning algorithm to predict ground shaking. In addition to the satisfactory accuracy and computational performance, such models can be easily extended to the prediction of additional metrics beyond ground shaking (such as building responses).

Machine learning algorithms and, in particular, ANN have been widely used in the past decade for the prediction of ground shaking (e.g., Derras *et al.*, 2014; Xie *et al.*, 2020). These algorithms can recognize complex nonlinear patterns in large datasets (Bishop, 2006) and do not rely on a specific functional form. Because of the abundance of open libraries, their application to ground-motion modeling is relatively straightforward and allows the consideration of a wide range of input parameters. The neural network used in this study is a feed-forward ANN with sequential layers made up of processing units performing

mathematical operations known as neurons (e.g., Haykin, 2009). Each neuron is described by a collection of synaptic weights and a bias, which collectively make up the neural network's parameters. The bias is a constant that is added to the result before it is transferred to the activation function, which is shared by all neurons in a given layer, and the synaptic weights are multipliers of the outputs of the preceding layer. The objective of the ANN training is to establish the parameters of the network by minimizing a loss function using the backpropagation algorithm. Additional information on the mathematical operations and characteristics of neural networks can be found in Perlovsky (2001), Bishop (2005), and Haykin (2009).

In the present study, the methodology described in Kalakonas and Silva (2022) was employed to train the ANN for ground-motion modeling using the widely applied mixed-effects approach. This methodology follows closely the algorithm proposed by Khosravikia and Clayton (2021), except for the likelihood maximization algorithm, which is adopted by Bates *et al.* (2015). In particular, the ANN parameters are calculated assuming a fixed-effects regression and the random effects, and their variances are estimated by likelihood maximization. The estimated between-event terms are subtracted from the simulated ground-motion data and the ANN is retrained on the updated database until the likelihood is maximized. Hence, the GMM can be expressed by the following formula (e.g., Joyner and Boore, 1993):

$$\ln(\text{IM}_{i,j}) = f(X, \theta) + \Delta B_i + \varepsilon_{i,j}, \quad (12)$$

in which $\ln(\text{IM}_{i,j})$ are the outputs of the ANN, which are typical IMs used in seismic risk assessment including PGA, PGV, and 5% damped SA for a total of 24 periods of vibration; X represents the input parameters (i.e., M_w , R_{JB} , and fault type [FT]); θ stands for the ANN parameters; $f(X, \theta)$ is the median prediction of the ground motion for an event i at site j ; ΔB_i is the event random-effect term accounting for the between-event variability for an event i ; and $\varepsilon_{i,j}$ is the residual term of the model representing the within-event variability for an event i at site j . According to Atik *et al.* (2010), these random-effect factors are taken to be independent random variables with standard normal distributions and standard deviations τ and ϕ . The total standard deviation can be calculated as follows:

$$\sigma = \sqrt{\tau^2 + \phi^2}. \quad (13)$$

Regarding the determination of the ANN hyperparameters (i.e., number of hidden layers and neurons, activation functions, etc.), the methodology proposed by Kalakonas and Silva (2021) was followed. In this process, the cross-validation approach is used to split the entire database into training and testing subsets and evaluate the model's performance. In particular, a fivefold cross-validation was utilized, in which the assembled database was divided arbitrarily into five equal

subsets (e.g., Khosravikia and Clayton, 2021; Kalakonas and Silva, 2022). Five ANNs were successively trained using four folds for training and one fold for testing the model's prediction on the omitted data. The average of the five trained ANNs was used to produce the cross-validation regression metrics, providing a reliable method to identify and prevent overfitting and underfitting. Each stage and modeling decision are summarized here for the sake of clarity and reproducibility:

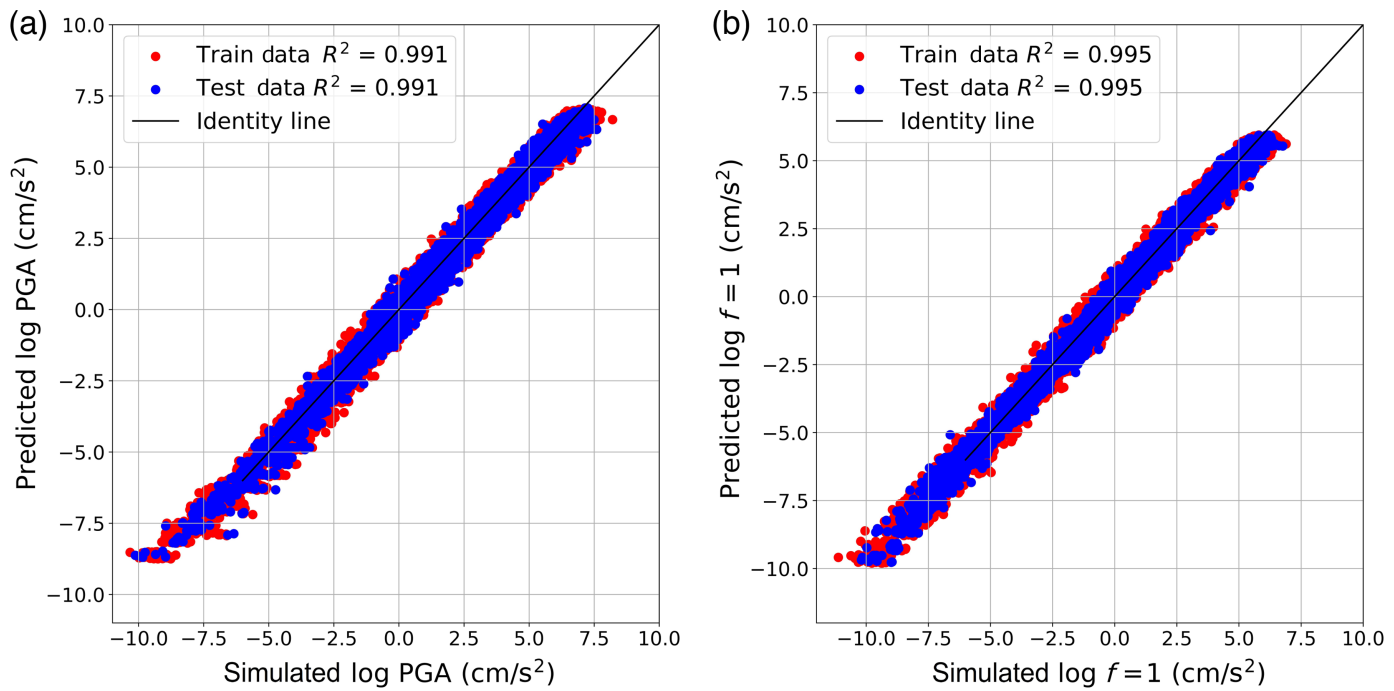
1. Preprocessing of input parameters and IMs: When the input and output data ranges are similar, ANN training is significantly more effective. For this reason, a one-hot encoding was used for FT, whereas the log10 was applied to R_{JB} (in kilometers), R (in kilometers), and all IMs (in centimeters, centimeter per second, and centimeter per second square).
2. Optimization algorithm and loss function: The mean square error (MSE) was selected as the loss function, which was minimized by the adaptive moment estimation algorithm (e.g., Kingma and Ba, 2014).
3. Number of hidden layers and activation functions: one hidden layer was used due to its sufficiency to approximate any real function according to the universal approximation theorem (e.g., Auer *et al.*, 2008). The hyperbolic tangent (\tanh) and the linear function were employed in the hidden and the output layers, respectively.
4. Number of neurons: The best number of neurons for the hidden layer was found by a trial-and-error process, leading to eight neurons, when more neurons resulted in overfitting.

We trained the neural network using the open-source library TensorFlow in a Python environment (e.g., Abadi *et al.*, 2016). Table 4 presents the average regression metrics for the five trained models. The evaluation of the potential over- or underfitting errors due to the choice of the hyperparameters was computed from the fixed-effect regression before the application of the mixed-effect algorithm. The results of the mixed-effects regression algorithm are presented in Table 5. The mathematical expression of the median prediction of the ANN for a given IM can be expressed by the following formula:

$$\overline{\ln(\text{IM}_j)} = f_{\text{lin}} \left(b_j + \sum_{h=1}^8 W_{j,h} \times \tanh \left(b_h + \sum_{i=1}^5 W_{i,h} X_i \right) \right), \quad (14)$$

in which X_i is the input parameter I ; $W_{i,h}$ is the weight of the hidden neuron h for the input X_i ; b_h is the bias of the hidden neuron h ; $W_{j,h}$ is the weight of the IM's neuron j for the output of neuron h ; b_j is the bias of the IM's neuron j ; and \tanh and f_{lin} are the activation functions of the hidden and output layer, respectively.

The R^2 coefficient is often used to measure the correlation between the recorded IMs and those predicted by the ML models (e.g., Dhanya and Raghukanth, 2018; Derakhshani and Foruzan,



2019; Khosravikia and Clayton, 2021). The simulated PGA and SA(1.0 s) values are displayed versus the results from the ANN in Figure 9. The ANN's predictive power was verified for all the ground-motion intensities, as demonstrated by the high R^2 values in Table 4. Additional analyses regarding the reliability of the resulting GMM are presented in the following section.

Figure 9. Stochastically simulated versus predicted correlation plot for (a) peak ground acceleration (PGA) and (b) spectral acceleration, SA, (1.0 s) using the entire database. The color version of this figure is available only in the electronic edition.

TABLE 4
Mean Regression Metrics of the Trained Artificial Neural Network (ANN) Models Using a Fivefold Cross Validation

T (s)	R ² Training	R ² Testing	MSE Training	MSE Testing
PGV	0.991	0.991	0.069	0.069
PGA	0.990	0.990	0.061	0.061
0.015	0.994	0.994	0.060	0.061
0.020	0.990	0.990	0.064	0.064
0.040	0.989	0.989	0.069	0.069
0.050	0.989	0.989	0.068	0.068
0.067	0.989	0.989	0.069	0.068
0.100	0.990	0.990	0.066	0.066
0.125	0.991	0.990	0.065	0.065
0.200	0.991	0.991	0.061	0.061
0.250	0.992	0.991	0.060	0.061
0.400	0.992	0.992	0.058	0.059
0.500	0.993	0.993	0.056	0.057
0.625	0.994	0.994	0.054	0.055
0.769	0.994	0.994	0.056	0.056
1.000	0.994	0.994	0.056	0.056
1.250	0.994	0.994	0.059	0.060
2.000	0.994	0.994	0.065	0.065
3.125	0.994	0.994	0.071	0.071
4.000	0.995	0.995	0.073	0.073

MSE, mean square error; PGA, peak ground acceleration; and PGV, peak ground velocity.

TABLE 5
Random-Effects Standard Deviation of the Selected Artificial Neural Network (ANN) Ground-Motion Model (GMM)

T (s)	Between-Event Variability (τ)	Within-Event Variability (ϕ)	Total Sigma (σ)
PGV	0.534	0.233	0.589
PGA	0.561	0.244	0.611
0.015	0.530	0.245	0.584
0.020	0.587	0.250	0.638
0.040	0.594	0.258	0.648
0.050	0.582	0.257	0.636
0.067	0.572	0.255	0.626
0.100	0.553	0.252	0.608
0.125	0.547	0.249	0.601
0.200	0.540	0.240	0.591
0.250	0.540	0.239	0.590
0.400	0.540	0.235	0.589
0.500	0.536	0.233	0.585
0.625	0.531	0.233	0.580
0.769	0.533	0.234	0.582
1.000	0.530	0.237	0.581
1.250	0.533	0.241	0.585
2.000	0.530	0.251	0.586
3.125	0.524	0.260	0.586
4.000	0.519	0.264	0.583

PGA, peak ground acceleration; and PGV, peak ground velocity.

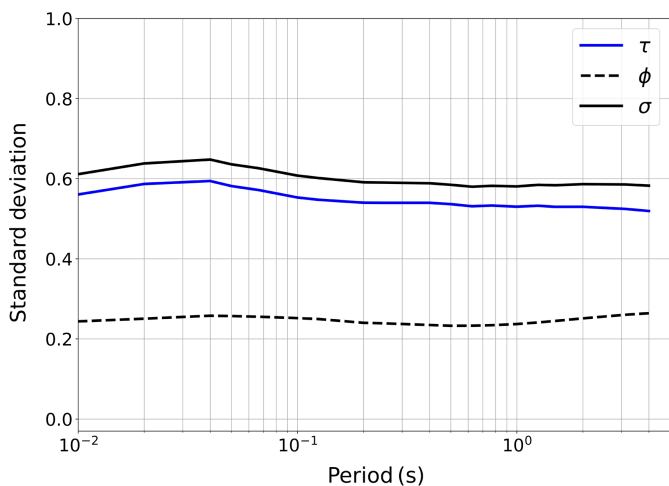


Figure 10. Standard deviation estimates of the components of aleatory uncertainty. The color version of this figure is available only in the electronic edition.

As previously explained, the aleatory uncertainty of the model was evaluated through the mixed-effect model. Figure 10 shows the between-event term, within-event term, and total standard deviations versus the period of vibration (T) in seconds. According to these results, the total sigma (σ) is dominated by the between-event term (τ) across all periods of vibration. This outcome contrasts with observations from other GMMs (e.g., Rodriguez-Marek *et al.*, 2011, Edwards and Fäh,

2013) in which usually the within-event term (ϕ) has a stronger influence on the total sigma. Drouet and Cotton (2015) performed a sensitivity analysis to study the effect of the uncertainty of all the modeling parameters used in the stochastic simulations in the GMM's uncertainty. They concluded that the major contributions to the total uncertainty come from the site amplification and κ_0 (which affect the within-event term) and from the stress parameter (which affects the between-event term). In the approach presented herein, simulation parameters are only sampled between the events (see Table 3). This will naturally lead to a large between-event variability, as all possible outcomes will be accounted for. Moreover, all the simulations in this study were performed assuming rock conditions (i.e., $V_{S30} = 760$ m/s), so the uncertainty due to site amplification is not accounted for in our analyses. Finally, we note that the κ_0 and attenuation parameters are not sampled within the sites. The same trend has been reported by other studies that also used a stochastic approach, which used the same assumptions, for the generation of the ground-motion recordings (e.g., Rietbroek *et al.*, 2013).

Figure 11 depicts the distributions of the between-event residuals (δE_i) for SA at two periods of vibration ($T = 0.2$ and 1.0 s) as a function of M_w . The error bars demonstrate the mean \pm standard deviation of the residuals for each M_w bin, according to a bin size of 0.5 units. For both IMs, it is possible to observe that the within-event and between-event residuals are close to zero for $M_w > 6.0$, whereas a small positive bias is observed for events of lower magnitude.

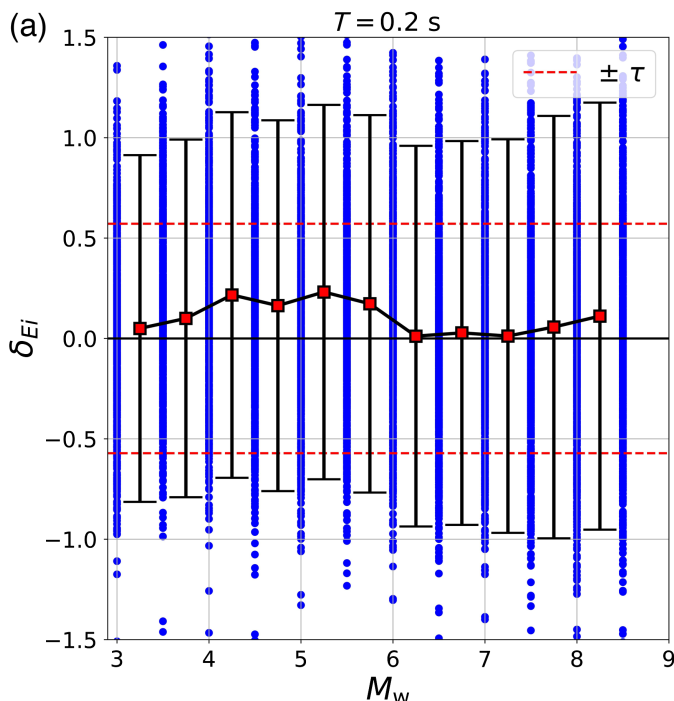
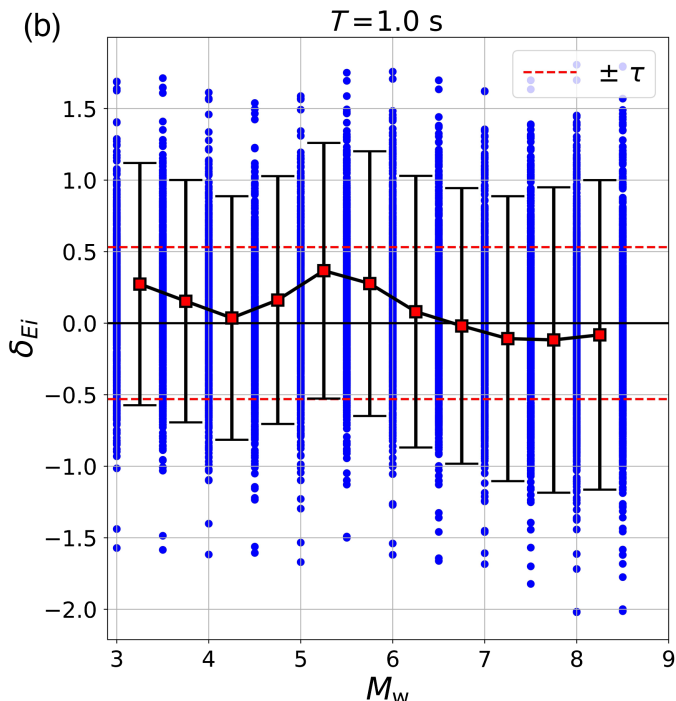
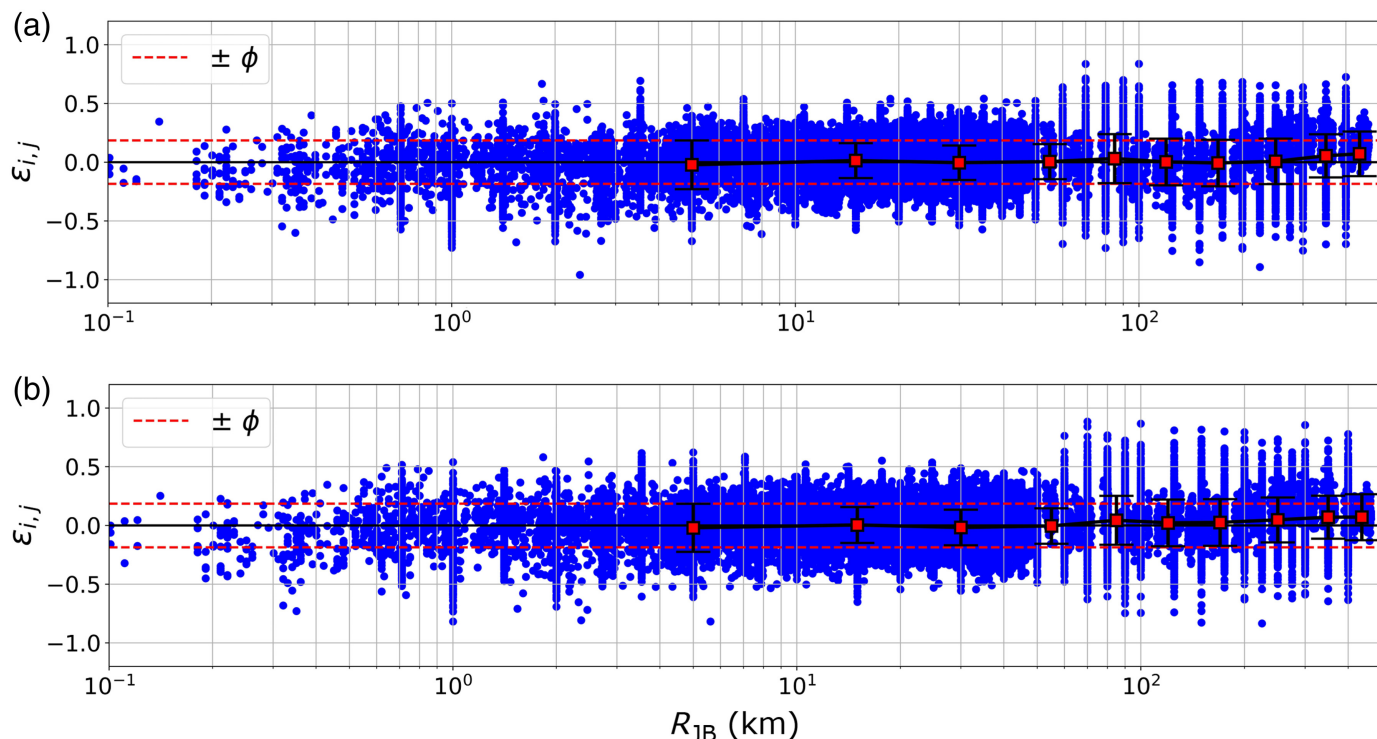


Figure 11. Distribution of the between-event terms with respect to M_w for (a) SA (0.2 s) and (b) SA (1.0 s). The magnitude has been binned every 0.5



M_w units and \pm one standard deviation are also plotted. The color version of this figure is available only in the electronic edition.



Finally, we present for both IMs the distribution of residuals ($\varepsilon_{i,j}$) versus distance (R_{JB}) in Figure 12. In both cases, the mean residuals are close to zero across all the distance bins, though a minor bias is observed for distances greater than 300 km.

The ANN along with the cross-validation and mixed-effects regression metrics are publicly available in a GitHub repository (see [Data and Resources](#)). This GMM will also be implemented directly within the OpenQuake engine ([Pagani et al., 2014](#)) to allow users to use it directly for seismic hazard and risk analysis.

DISCUSSION OF RESULTS

Comparison with other GMMs

This section presents a comparison between common GMMs for SCRs and the model proposed herein. These models have been developed for ENA, Australia, Germany, and Switzerland, as well as for other European regions characterized by low-to-moderate

Figure 12. Distribution of the residual terms with respect to R_{JB} for the two selected IMs: (a) SA (0.2 s), and (b) SA (1.0 s). The magnitude has been binned every 0.5 M_w units and \pm one standard deviation are also plotted. The color version of this figure is available only in the electronic edition.

seismicity and slow ground-motion attenuation ([Kotha et al., 2020](#)). Information such as geographic applicability, reference soil conditions, and faulting type for each model is presented in Table 6.

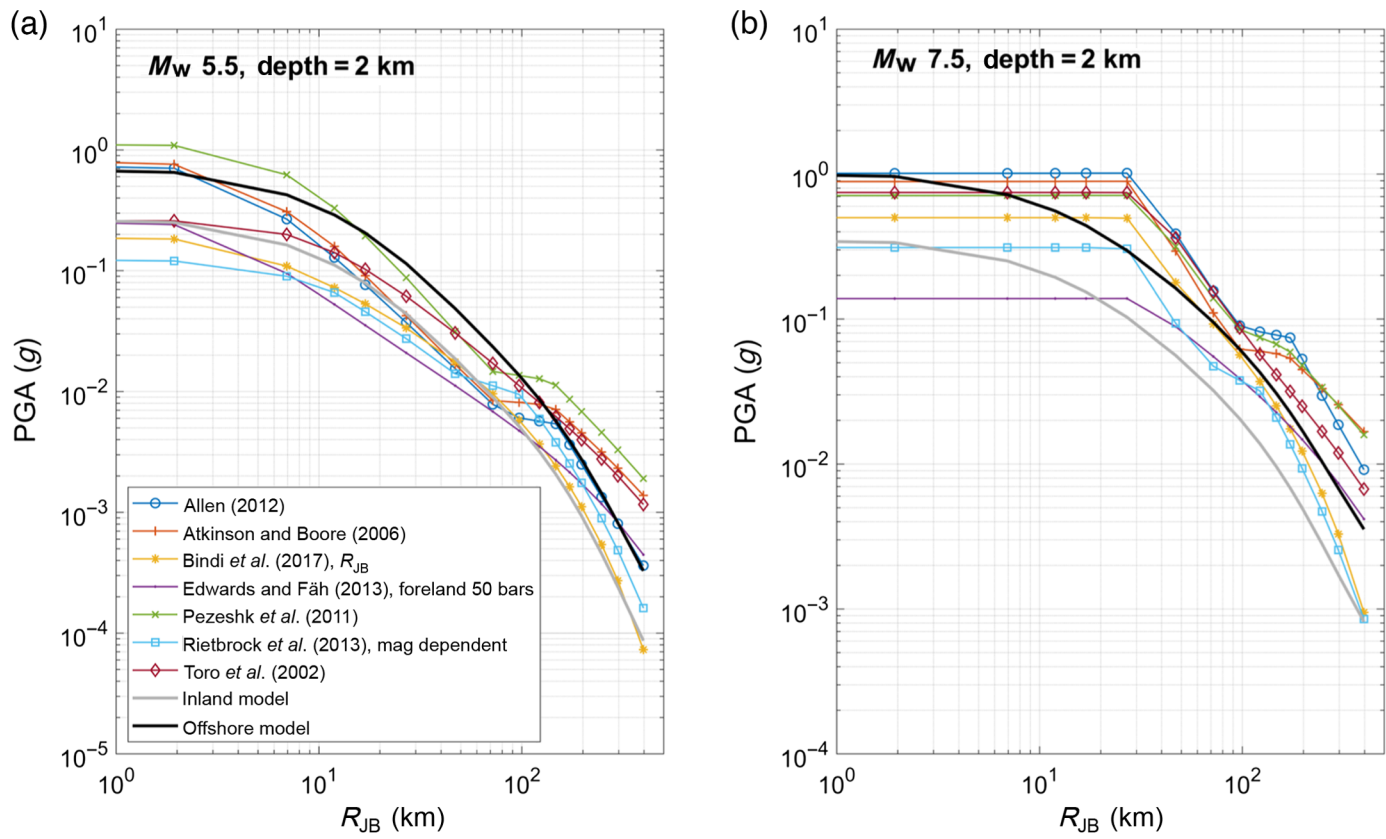
Figures 13 and 14 present the PGA and SA at 1.0 s, respectively, as a function of distance (R_{JB}) for two events (M_w 5.5 and 7.5), considering the GMMs listed in Table 6. It should be noted that all the comparisons were carried out considering rock conditions ($V_{S30} = 760$ m/s). In all cases, the faulting mechanism was assumed to be reversed and the rupture depth equal to 2 km.

The difference in the results for the inland and offshore scenarios is evident in all the figures. This is an expected

TABLE 6
Candidate Ground-Motion Prediction Equations (GMPEs) Selected for Comparisons with the Model Derived in this Study

Reference	Geographic Applicability	Intensity Measure	Reference Soil Condition	Faulting Mechanism
Toro et al. (1997, 2002)	ENA	SA, PGV	Hard rock, $V_S = 2800$ m/s	Reverse, strike slip
Atkinson and Boore (2006)	ENA	SA, PGV	Rock, $V_S = 760$ m/s	Reverse, strike slip
Pezeshk et al. (2011)	ENA	SA	Hard rock, $V_S \geq 2000$ m/s	Reverse, strike slip
Allen (2012)	Australia	SA	Rock, $V_S = 760$ m/s	NA
Rietbrock et al. (2013)	United Kingdom	SA, PGV	Hard rock, $V_S = 2300$ m/s	Strike slip
Edwards and Fäh (2013)	Switzerland	SA, PGV	Rock, $V_S = 1105$ m/s	Normal, strike slip
Bindi et al. (2017)	Germany	SA	Rock, $V_S = 800$ m/s	Normal, reverse, and strike slip

ENA, eastern North America; PGV, peak ground velocity; and SA, spectral acceleration.



outcome given the differences in the main input parameters defined for these two regions (see Table 2). From the figures, it can be observed that, at distances below 15 km, where the stress drop controls the ground motions, the inland model is closer to the GMM developed by Rietbrock *et al.* (2013) and Edwards and Fäh (2013), whereas the offshore model produces values closer to the ENA models at this range of distance. The difference between the two models can be explained by the selected value of stress drop. At intermediate distances, the differences between the models are due to the different geometrical spreading functions defined for each model. For the offshore model, the ground motion values decrease with distance at a lower rate. This trend is due to the lower geometrical spreading coefficient assumed for the offshore model at this range of distance. For distances above 100 km, a higher attenuation is evident for the model presented herein compared to other models. This is due to the lower Q values in our region of interest. Our results suggest that the GMMs developed for ENA tend to overpredict ground shaking for inland earthquakes in southwest Iberia but led to results relatively similar to the ones presented herein for the offshore scenario. It is important to mention that offshore events occur mostly at distances of 100 km south and southwest of our region of interest, and thus their performance at distances below this threshold is less relevant. This performance is further discussed in the following section.

Figures 15 and 16 depict the median response spectra predicted for two magnitudes (M_w 5.5 and 7.5) at three different

Figure 13. IM- R_{JB} attenuation curve for PGA and comparison with other ground-motion models (GMMs) assuming (a) M_w 5.5, and (b) M_w 7.5 and a depth of 2 km. The color version of this figure is available only in the electronic edition.

distances. The SA values are calculated for the rock site ($V_{S30} = 760$ m/s) at 2 km depth. For the M_w 5.5 scenario, except for periods below 0.1 s, the offshore model predicts similar values. At short distances ($R_{JB} = 10$ km), the spectral shape of the offshore model at high frequencies (periods below 0.1) is different from ENA models (e.g., Atkinson and Boore, 2006), which can be a result of the assumption of higher values for the spectral decay factor κ_0 in our model. However, because period increases the offshore model aligns closely with ENA models. At moderate distances ($R_{JB} = 50$ km), the offshore model tends to overpredict the pseudospectral acceleration (PSA) compared to other models. This is a result of the assumption of a lower geometrical spreading coefficient at short distances in our model. As discussed earlier, the performance of the offshore model in distances below 100 km was affected by the lack of data in this range. Nevertheless, at larger distances ($R_{JB} = 200$ km), the offshore model predicts values relatively close to Atkinson and Boore (2006) model. In contrast, the spectral shape and values generated by our Inland model exhibit relative similarity to other European models that employ similar stress-drop values (e.g. Edwards and Fäh, 2013; Rietbrock *et al.*, 2013). However, at short distances

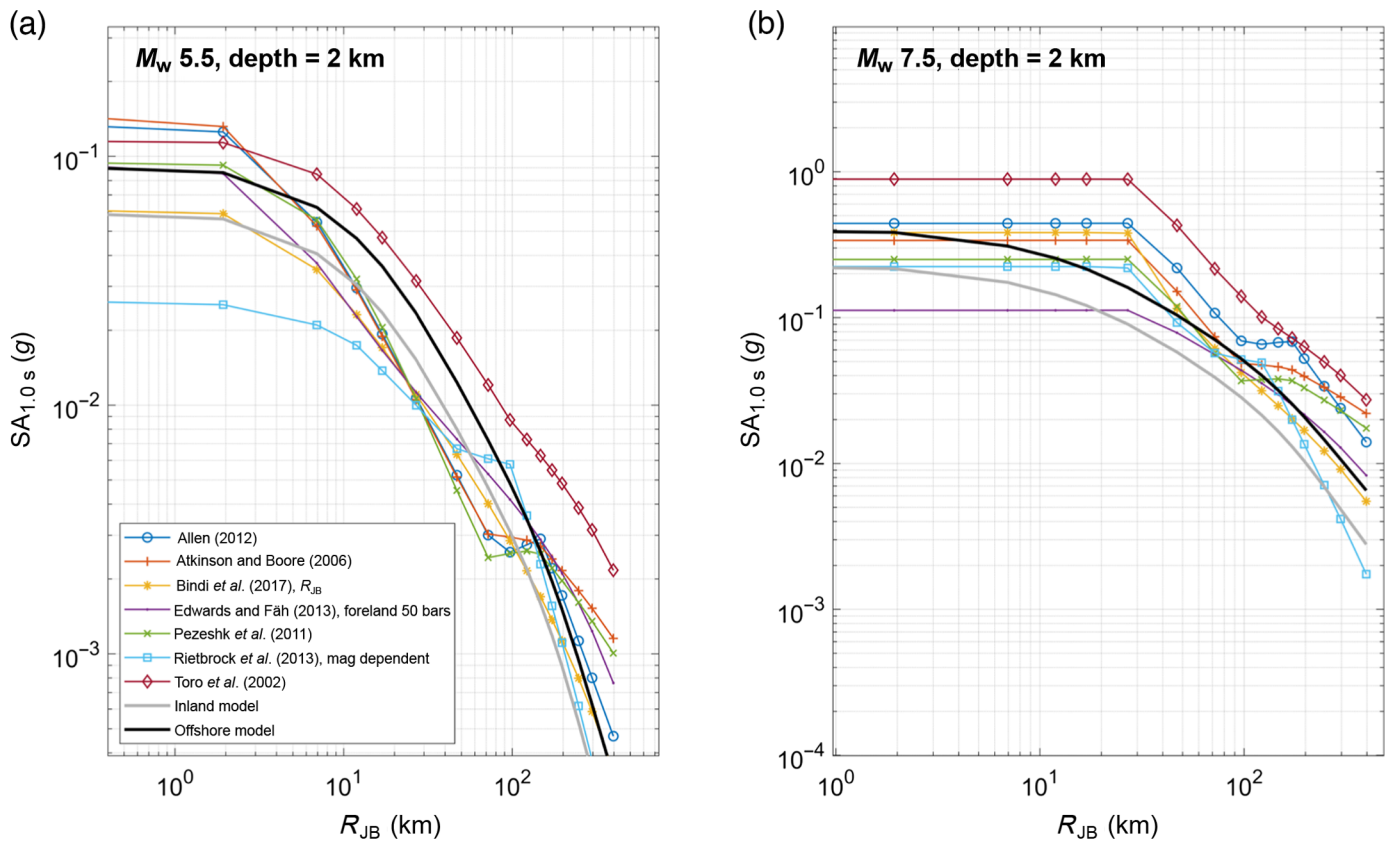


Figure 14. IM- R_{JB} attenuation curve for SA (1.0 s) and comparison with other GMMs assuming (a) M_w 5.5, and (b) M_w 7.5 and a depth of

2 km. The color version of this figure is available only in the electronic edition.

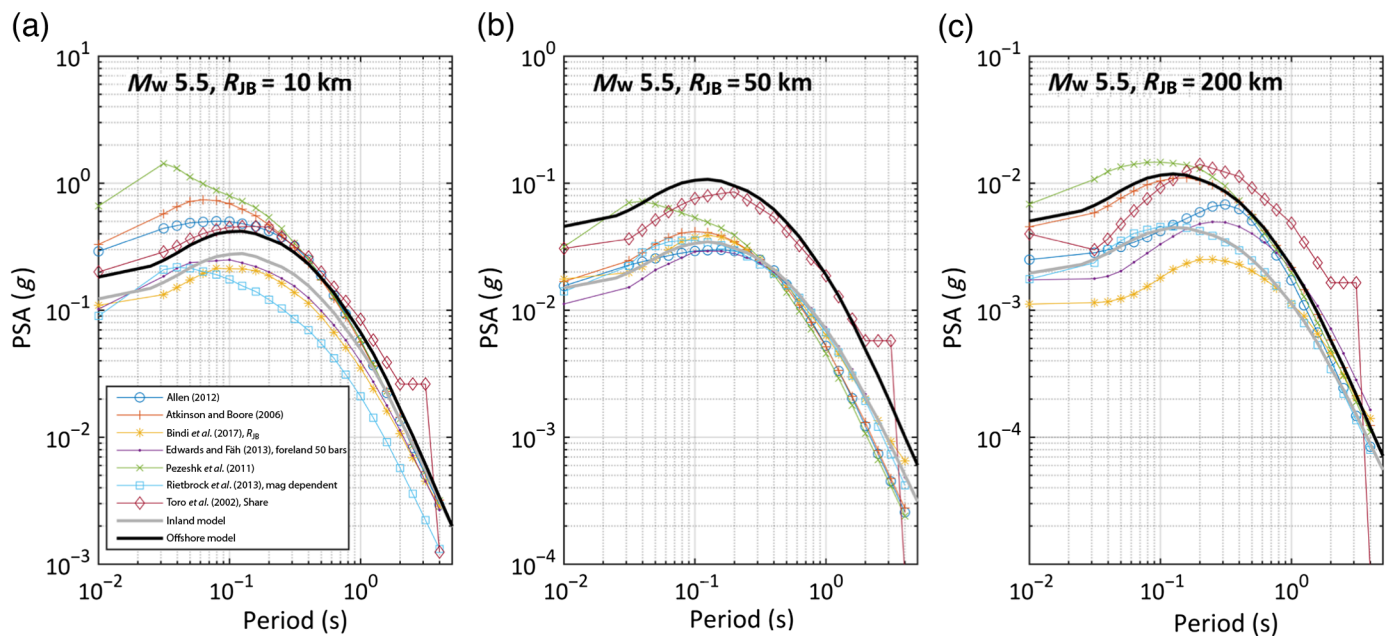


Figure 15. Comparison of median spectral acceleration (SA) generated using the proposed models and other existing GMMs assuming M_w 5.5 and three different distances: (a) $R_{JB} = 10$ km, (b) $R_{JB} = 50$ km, and

(c) $R_{JB} = 200$ km. The color version of this figure is available only in the electronic edition.

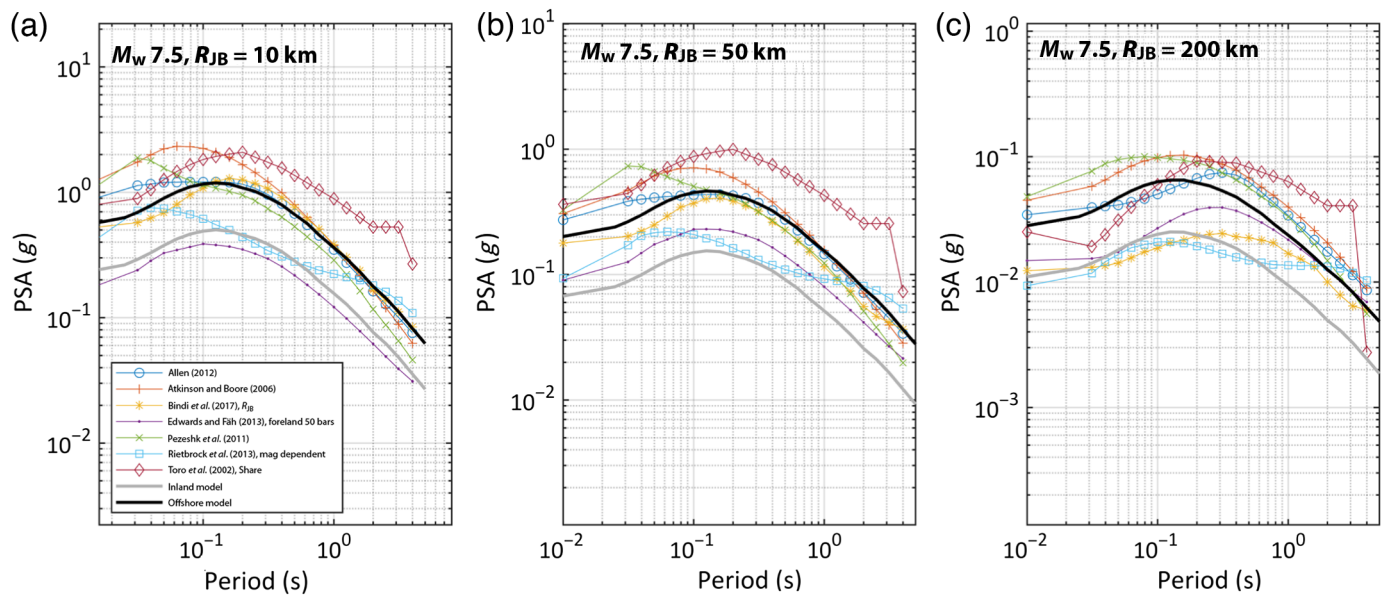


Figure 16. Comparison of median SA generated using the proposed models and other existing GMMs assuming M_w 7.5 and three different distances

(a) $R_{JB} = 10, (b) $R_{JB} = 50, and (c) $R_{JB} = 200. The color version of this figure is available only in the electronic edition.$$$

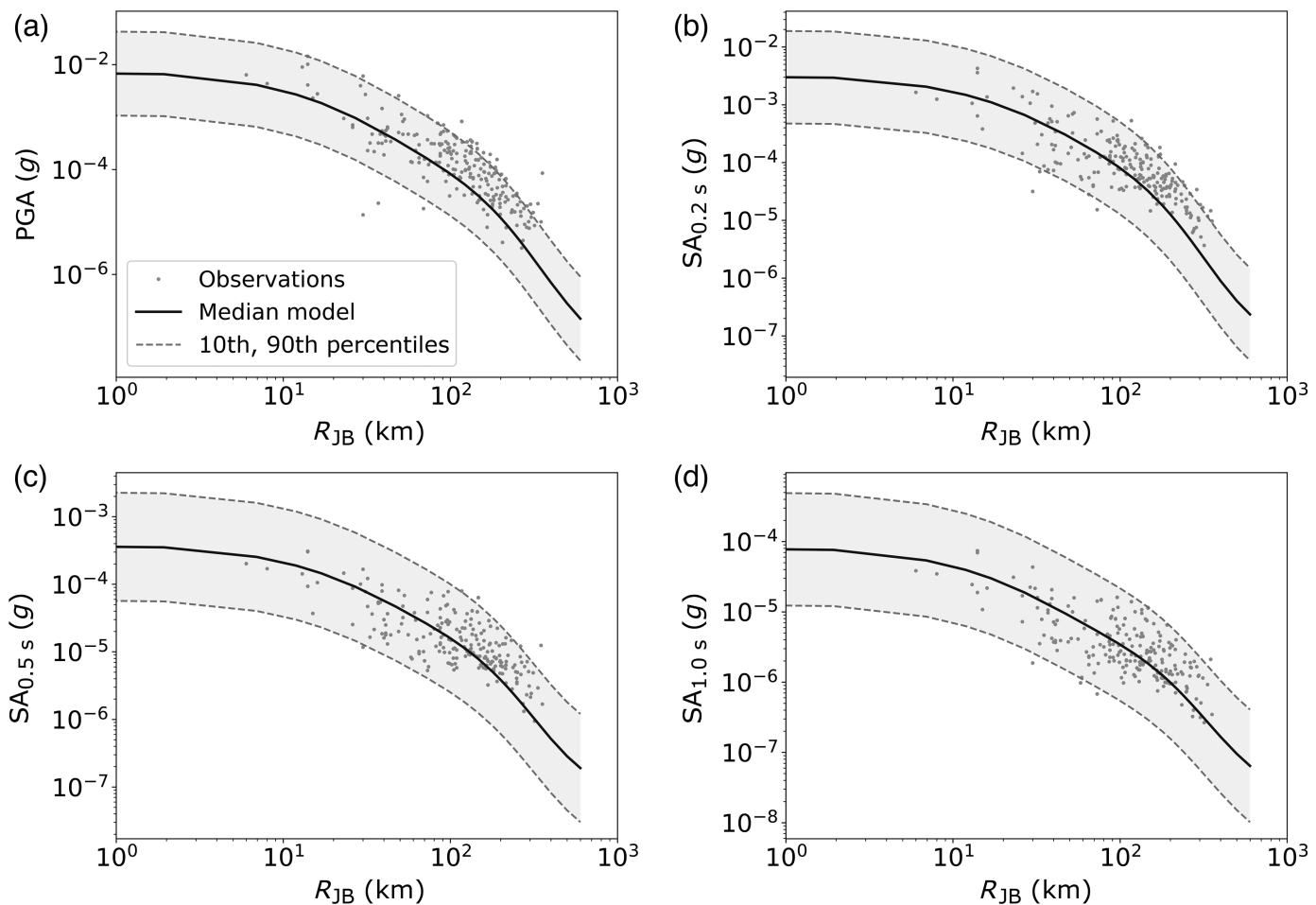
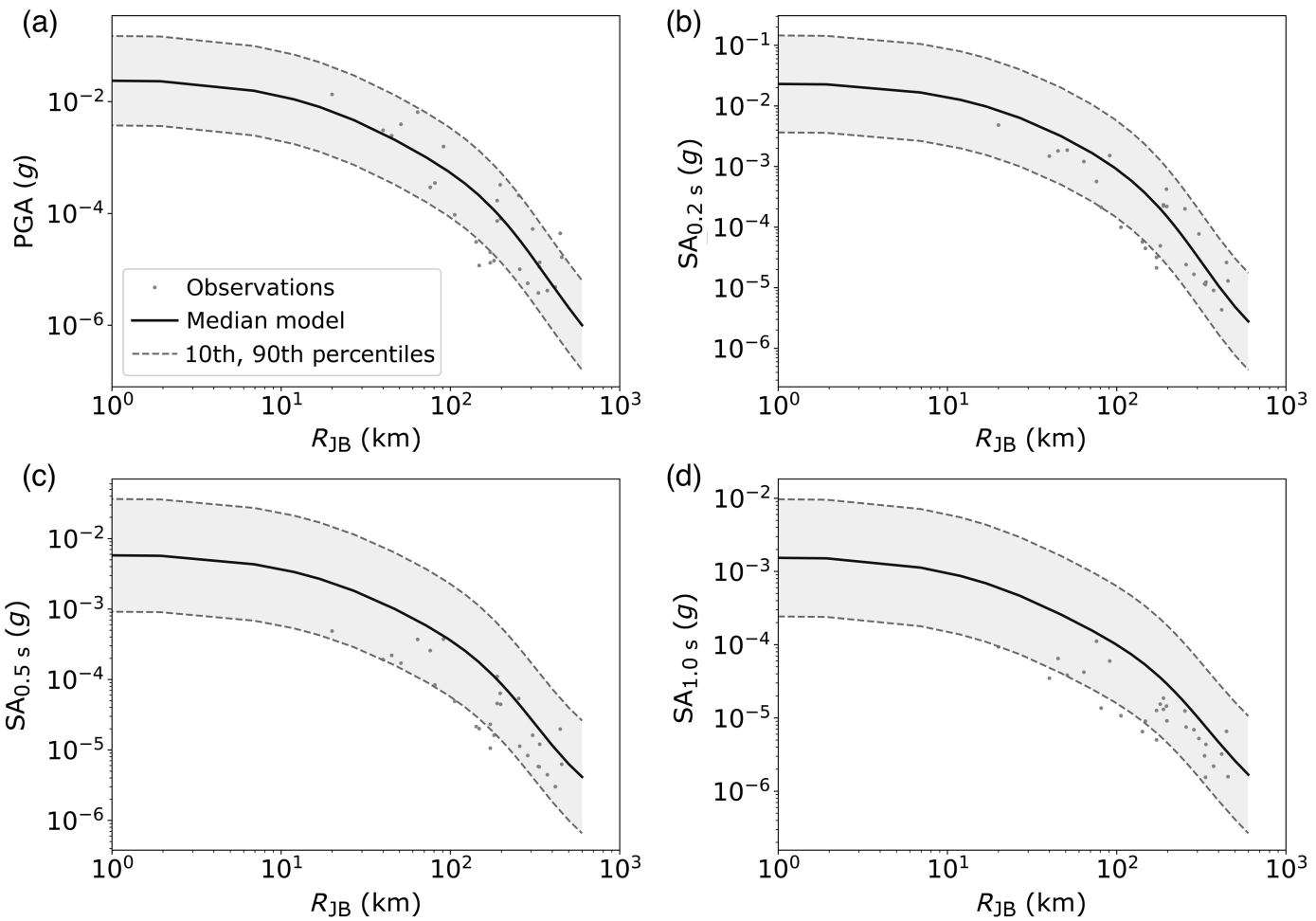


Figure 17. Attenuation of four selected IMs: (a) PGA, (b) SA (0.2 s), (c) SA (0.5 s), (d) SA (1.0 s), based on an inland model assuming M_w 3 compared with empirical data from past inland events in the region.

The gray dots represent observations for M_w 3 inland events in the region. The shaded areas indicate the corresponding uncertainty range of the predictions.



($R_{JB} = 10$ km), our Inland model predicts higher PSA across all period ranges. At distances $R_{JB} = 50$ km and $R_{JB} = 200$ km, the PSA predicted by the inland model aligns with those of the [Rietbrock et al. \(2013\)](#) model.

In the case of M_w 7.5 events the spectral shape of the offshore model deviates from ENA models (e.g., [Atkinson and Boore, 2006](#)), displaying underestimation by a factor of 2 at periods below 0.5 s. However, at short-to-moderate distances, the offshore model is relatively close to [Atkinson and Boore \(2006\)](#), by a 15% difference. In this case, no specific comparable trend is observed between the inland model and European models. At a moderate distance, $R_{JB} = 50$ km; however, the inland model is relatively closer to the GMMs developed by [Edwards and Fäh \(2013\)](#) and [Rietbrock et al. \(2013\)](#). The difference between models in the case of M_w 7.5 scenarios can be a result of the different magnitude saturation of the models.

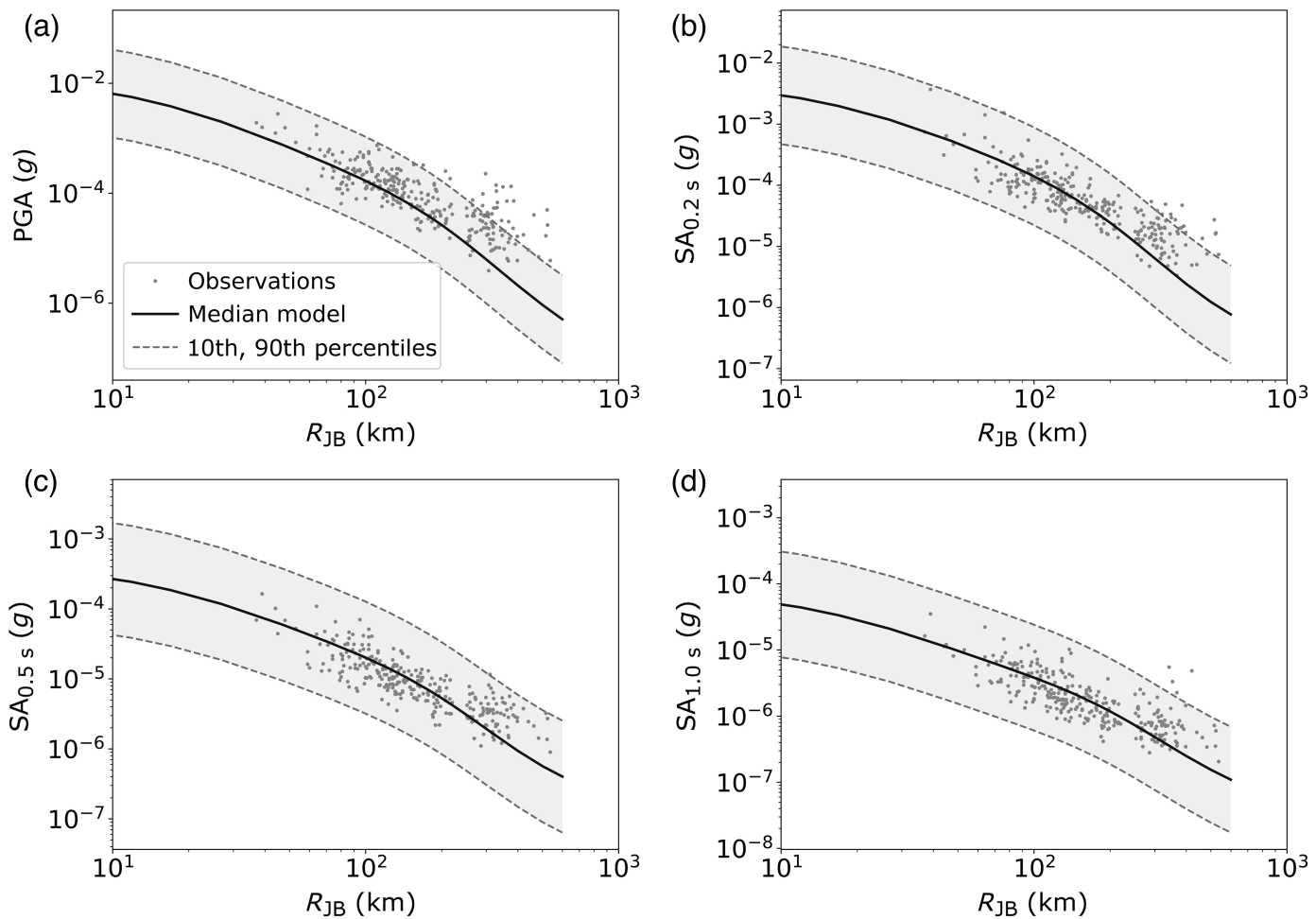
Comparison with ground-motion recordings

We used ground-motion recordings from past earthquakes in southwest Iberia to evaluate the accuracy and reliability of our predictions. As stated earlier, these data correspond to low-to-moderate magnitude events in the region. Figures 17–20

Figure 18. Attenuation of four selected IMs: (a) PGA, (b) SA (0.2 s), (c) SA (0.5 s), (d) SA (1.0 s), based on an inland model assuming M_w 4 compared with empirical data from past inland events in the region. The gray dots represent observations for M_w 4 inland events in the region. The shaded areas indicate the corresponding uncertainty range of the predictions.

present four intensity measures for inland and offshore events with different magnitudes. In general, a satisfactory agreement between our predictions and the recorded data is observed, except the M_w 4 (Fig. 18) in which an overestimation for SA (0.5 s) and SA (1.0 s) is observed, as well as the M_w 3 events where a slight underestimation of PGA and SA (0.2 s) for distances above 100 km can be observed. These results indicate that most of the observations are within the 10th and 90th uncertainty range of the proposed model.

Finally, Figure 21 compares the acceleration response spectra for the offshore model with the waveforms recorded from two M_w 6.0 earthquakes at stations with different distances (from 180 to 270 km). In all cases, the offshore model can predict the SA within the entire range of periods with a relatively good agreement.



CONCLUSIONS

In this study, the well-known finite-fault stochastic ground-motion simulation approach has been used to generate synthetic records for a large number of hypothetical scenarios in southwest Iberia. These records were used to calibrate a new ANN-based GMM to predict ground-shaking IMs such as PGA, PGV, and SA on rock conditions ($V_{S30} = 760$ m/s) for inland and offshore earthquakes in the region.

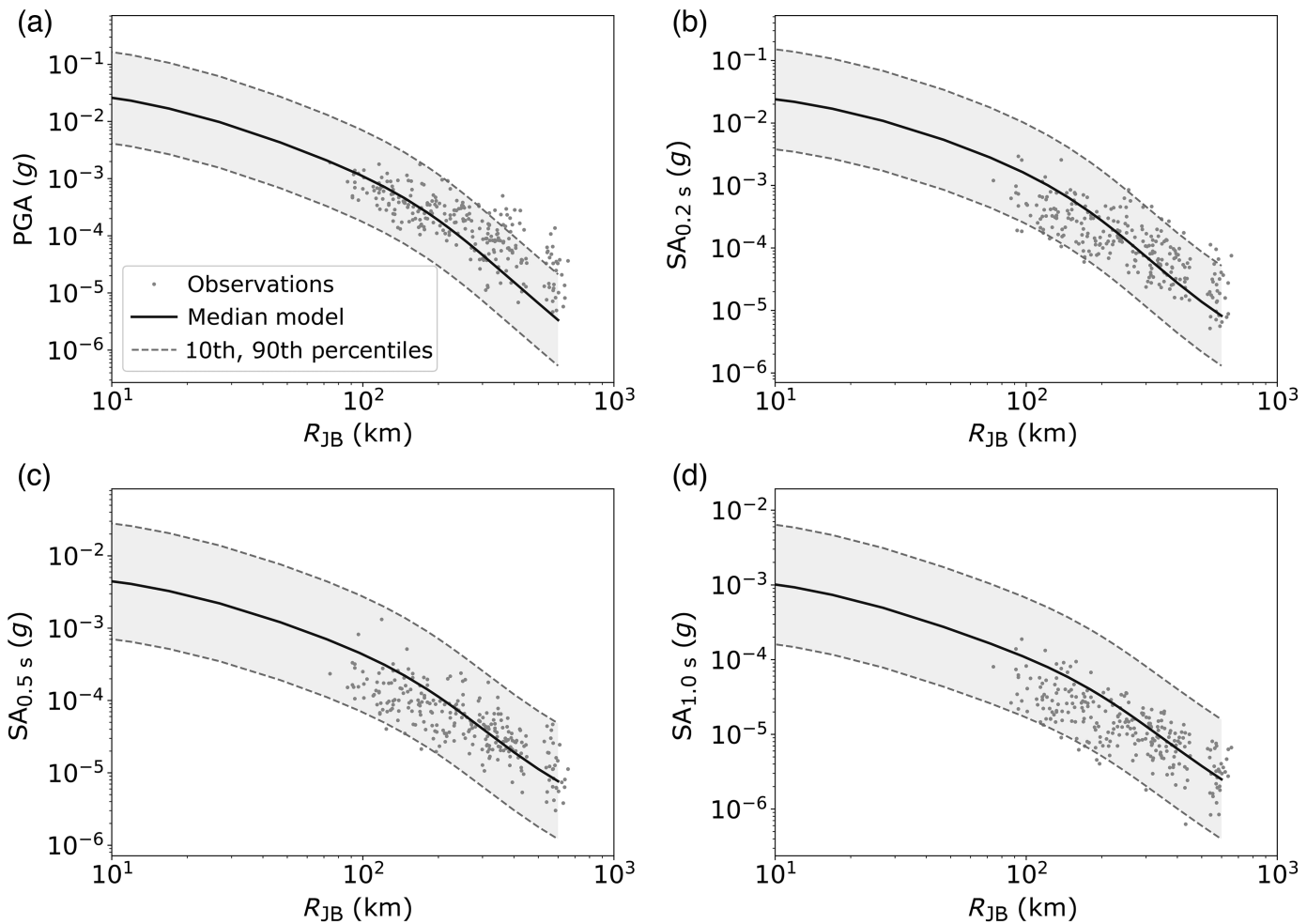
Taking into account the variation in geometrical and anelastic attenuation as well as the variations in stress drop ($\Delta\sigma$) in the region, the proposed GMM accounts for the location of the event (inland and offshore). The empirical ground-motion records from past earthquakes in the region were extracted from local databases (IPMA and IGN) and were employed to calibrate the simulation parameters. It was found that to reproduce the SA values from past earthquakes recorded in offshore Iberia, it is necessary to have a considerably greater stress drop (to the order of 3.0), in comparison with the inland earthquakes. The aleatory uncertainty values for the most important simulation parameters were adopted from [Atkinson and Boore \(2006\)](#).

The regression analysis of the simulated ground-motion values was carried out following the mixed-effects approach

Figure 19. Attenuation of four selected IMs: (a) PGA, (b) SA (0.2 s), (c) SA (0.5 s), (d) SA (1.0 s), based on an offshore model assuming M_w 3 compared with empirical data from past offshore events in the region. The gray dots represent observations for M_w 3 offshore events in the region. The shaded areas indicate the corresponding uncertainty range of the predictions.

and the ANN algorithm proposed by [Khosravikia and Clayton \(2021\)](#). The input parameters for the regression model are M_w , R_{JB} , R, FM, and location of the event. The outputs are the median values of the predicted IMs and the associated uncertainty. The total ground-motion sigma was divided into between-event and within-event terms.

The developed models were compared with the existing GMMs for other SCRs as well as the available models for low-to-moderate hazard regions in Europe, some of which have been used in the past in seismic hazard and risk analysis for the country. In general, we note that most models tend to underestimate the ground shaking for offshore events and overestimate for inland events. This trend could mean that the seismic hazard due to inland seismicity might be overestimated, whereas the contribution of the offshore events to the National Seismic Hazard and Risk could be underestimated.



The model presented herein can be used in future Seismic Hazard and Risk Assessment studies for southwest Iberia. However, we note that the proposed model provides ground shaking for rock conditions, and for the assessment of earthquake damage and losses, it is fundamental to account for site conditions (e.g., Acevedo *et al.*, 2020). The evaluation of ground-shaking amplification was out of the scope of this study. Instead, we recommend using one of the existing amplification models in the literature, such as Stewart *et al.* (2020) or Weatherill *et al.* (2022). We also note for the inversion of stochastic parameters, we used common derivation methodologies applied in several past studies, but more recent methodologies have been proposed for the estimation of stress drop (e.g., Baltay *et al.*, 2019; Trugman, 2020) and attenuation parameters (e.g., Shible *et al.*, 2022). There are still limitations in different parts of the model due to the paucity of recorded data from past earthquakes. Improvements and expansion of the existing strong-motion networks will provide better-recorded data, especially in case of offshore events, which can enable testing and further improvement of the proposed GMM. In addition, this study does not account for the effects of epistemic uncertainty in the simulation parameters. Further research is required to explore how this uncertainty impacts the ground-motion simulations in the region.

Figure 20. Attenuation of four selected IMs: (a) PGA, (b) SA (0.2 s), (c) SA (0.5 s), (d) SA (1.0 s), based on an offshore model assuming M_w 4 compared with empirical data from past offshore events in the region. The gray dots represent observations for M_w 4 offshore events in the region. The shaded areas indicate the corresponding uncertainty range of the predictions.

DATA AND RESOURCES

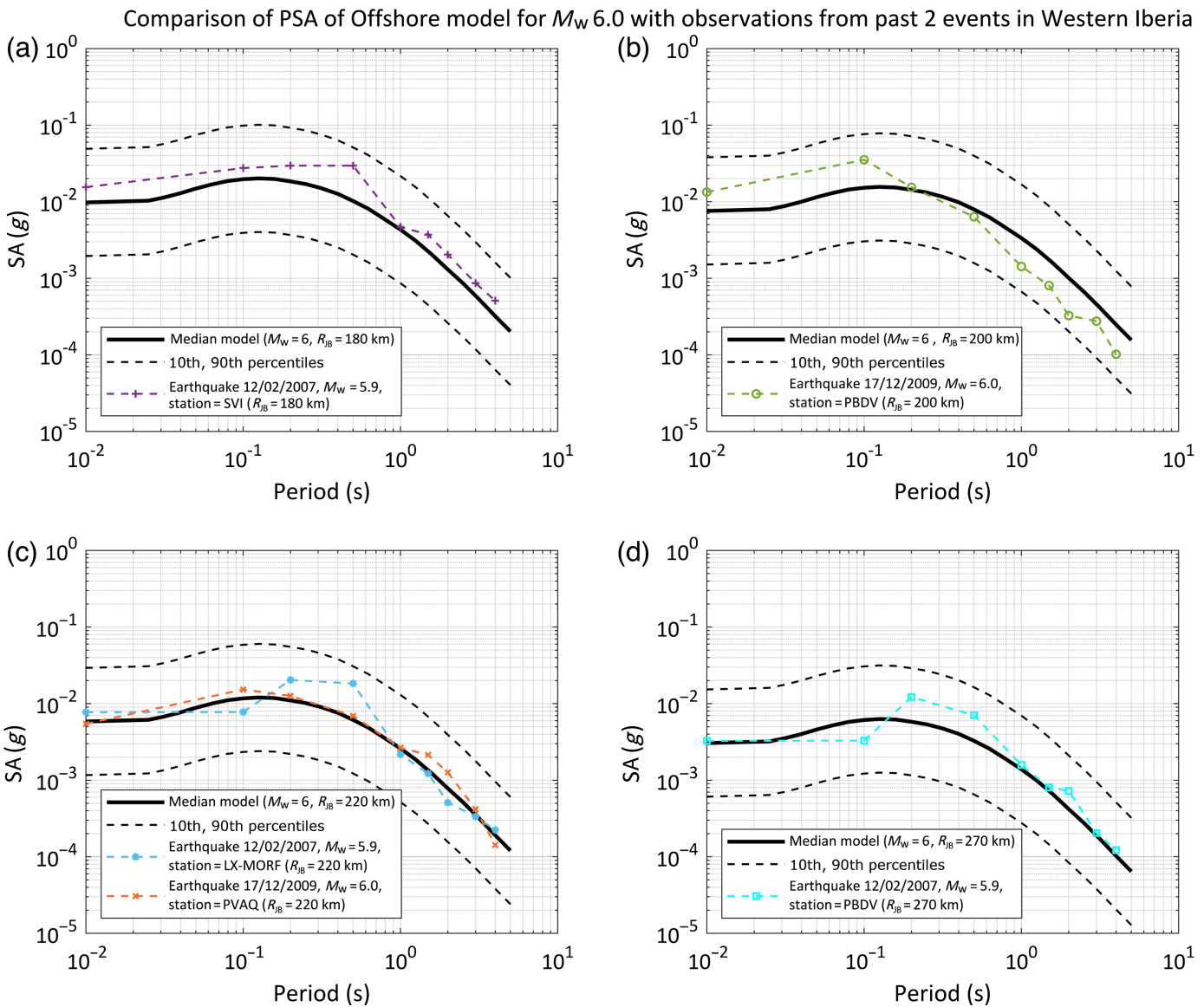
The earthquake catalog and seismic signals used in this study can be found in the following links: <http://ceida.ipma.pt/web-interface/> (last accessed January 2024) and <https://www.ign.es/web/ign/portal/sis-catalogo-acelerogramas> (last accessed January 2024). The artificial neural network (ANN) model along with the cross-validation and mixed-effects regression metrics developed in this study are publicly available through a GitHub repository <https://github.com/amirt1994/ANN-Ground-Motion-Model-for-Western-Iberia> and <https://github.com/amirt1994> (last accessed May 2024).

DECLARATION OF COMPETING INTERESTS

The authors acknowledge that there are no conflicts of interest recorded.

ACKNOWLEDGMENTS

This study was supported by the Foundation for Science and Technology (FCT) in the framework of the research project ASSIMILATE—Assessment of Seismic Safety Integrated with Machine Learning and



Tremors PTDC/ECI-EGC/7244/2020. The authors thank the Associate Editor and three anonymous reviewers for their constructive comments which helped improve this article. The first author acknowledges FCT for the grant with reference 2022.12609.BD. The first author thanks Navid Kheirdast for his help in the raw data processing.

REFERENCES

- Abadi, M., A. Agarwal, P. Barham, E. Brevdo, Z. Chen, C. Citro, G. S. Corrado, A. Davis, J. Dean, M. Devin, *et al.* (2016). TensorFlow: Large-scale machine learning on heterogeneous distributed systems, doi: [10.48550/arXiv.1603.04467](https://doi.org/10.48550/arXiv.1603.04467).
- Acevedo, A. B., C. Yepes-Estrada, D. González, V. Silva, M. Mora, M. Arcila, and G. Posada (2020). Seismic risk assessment for the residential buildings of the major three cities in Colombia: Bogotá, Medellín, and Cali, *Earthq. Spectra* **36**, 298–320, doi: [10.1177/8755293020942537](https://doi.org/10.1177/8755293020942537).
- Aki, K. (1972). Earthquake mechanism, *Tectonophysics* **13**, 423–446, doi: [10.1016/0040-1951\(72\)90032-7](https://doi.org/10.1016/0040-1951(72)90032-7).
- Akkar, S., and J. J. Bommer (2010). Empirical equations for the prediction of PGA, PGV and spectral accelerations in Europe, the Mediterranean region and the Middle East, *Seismol. Res. Lett.* **81**, 195–206, doi: [10.1785/gssrl.81.2.195](https://doi.org/10.1785/gssrl.81.2.195).
- Allen, T. I. (2012). Stochastic ground-motion prediction equations for southeastern Australian earthquakes using updated source and attenuation parameters, available at <https://ecat.ga.gov.au/geonet/work/srv/api/records/c12439e0-a255-5972-e044-00144fdd4fa6> (last accessed January 2024).
- Allen, T. I., P. R. Cummins, T. Dhu, and J. F. Schneider (2007). Attenuation of ground-motion spectral amplitudes in southeastern Australia, *Bull. Seismol. Soc. Am.* **97**, no. 4, 1279–1292, doi: [10.1785/0120060172](https://doi.org/10.1785/0120060172).
- Allmann, B. P., and P. M. Shearer (2009). Global variations of stress drop for moderate to large earthquakes, *J. Geophys. Res.* **114**, B01310, doi: [10.1029/2008JB005821](https://doi.org/10.1029/2008JB005821).

- Amaro-Mellado, J. L., D. Antón, and J. M. Alcalde (2021). GIS-based study of the evolution of the IGN's strong motion network of mainland Spain and the Balearics, *Geodes. Geodynam.* **12**, 279–287, doi: [10.1016/J.GEOG.2021.06.003](https://doi.org/10.1016/J.GEOG.2021.06.003).
- Ambraseys, N. N., J. Douglas, S. K. Sarma, and P. M. Smit (2005). Equations for the estimation of strong ground motion from shallow crustal earthquakes using data from Europe and the Middle East: Horizontal peak ground acceleration and spectral acceleration, *Bull. Earthq. Eng.* **3**, 1–53, doi: [10.1007/s10518-005-0183-0](https://doi.org/10.1007/s10518-005-0183-0).
- Anderson, J. G., and S. E. Hough (1984). A model for the shape of the Fourier amplitude spectrum of acceleration at high frequencies, *Bull. Seismol. Soc. Am.* **74**, 1969–1993.
- Assatourians, K., and G. M. Atkinson (2007). Modeling variable-stress distribution with the stochastic finite-fault technique, *Bull. Seismol. Soc. Am.* **97**, 1935–1949, doi: [10.1785/0120060203](https://doi.org/10.1785/0120060203).
- Atik, L. A., N. Abrahamson, J. J. Bommer, F. Scherbaum, F. Cotton, and N. Kuehn (2010). The variability of ground-motion prediction models and its components, *Seismol. Res. Lett.* **81**, 794–801, doi: [10.1785/gssrl.81.5.794](https://doi.org/10.1785/gssrl.81.5.794).
- Atkinson, G. M. (2004). Empirical attenuation of ground-motion spectral amplitudes in southeastern Canada and the northeastern United States, *Bull. Seismol. Soc. Am.* **94**, 1079–1095, doi: [10.1785/0120030175](https://doi.org/10.1785/0120030175).
- Atkinson, G. M., and I. Beresnev (1997). Don't call it stress drop, *Seismol. Res. Lett.* **68**, 1–4.
- Atkinson, G. M., and D. M. Boore (1995). Ground-motion relations for eastern North America, *Bull. Seismol. Soc. Am.* **85**, 17–30, doi: [10.1785/BSSA0850010017](https://doi.org/10.1785/BSSA0850010017).
- Atkinson, G. M., and D. M. Boore (2006). Earthquake ground-motion prediction equations for eastern North America, *Bull. Seismol. Soc. Am.* **96**, 2181–2205, doi: [10.1785/0120050245](https://doi.org/10.1785/0120050245).
- Atkinson, G. M., and R. F. Mereu (1992). The shape of ground motion attenuation curves in southeastern Canada, *Bull. Seismol. Soc. Am.* **82**, 2014–2031, doi: [10.1785/BSSA0820052014](https://doi.org/10.1785/BSSA0820052014).
- Auer, P., H. Burgsteiner, and W. Maass (2008). A learning rule for very simple universal approximators consisting of a single layer of perceptrons, *Neural Netw.* **21**, 786–795, doi: [10.1016/j.neunet.2007.12.036](https://doi.org/10.1016/j.neunet.2007.12.036).
- Baltay, A. S., T. C. Hanks, and N. A. Abrahamson (2019). Earthquake stress drop and Arias intensity, *J. Geophys. Res.* **124**, 3838–3852.
- Bates, D., M. Mächler, B. Bolker, and S. Walker (2015). Fitting linear mixed-effects models using lme4, *J. Stat. Software* **67**, 1–48, doi: [10.18637/jss.v067.i01](https://doi.org/10.18637/jss.v067.i01).
- Bay, F., D. Fäh, L. Malagnini, and D. Giardini (2003). Spectral shear-wave ground-motion scaling in Switzerland, *Bull. Seismol. Soc. Am.* **93**, 414–429.
- Beyreuther, M., R. Barsch, L. Krischer, T. Megies, Y. Behr, and J. Wassermann (2010). ObsPy: A Python toolbox for seismology, *Seismol. Res. Lett.* **81**, 530–533, doi: [10.1785/gssrl.81.3.530](https://doi.org/10.1785/gssrl.81.3.530).
- Bindi, D., F. Cotton, S. R. Kotha, C. Bosse, D. Stromeyer, and G. Grünthal (2017). Application-driven ground motion prediction equation for seismic hazard assessments in non-cratonic moderate-seismicity areas, *J. Seismol.* **21**, 1201–1218, doi: [10.1007/s10950-017-9661-5](https://doi.org/10.1007/s10950-017-9661-5).
- Bishop, C. M. (2005). *Neural Networks for Pattern Recognition*, Oxford University Press, New York.
- Bishop, C. M. (2006). *Pattern Recognition and Machine Learning*, Springer, New York.
- Boore, D. M. (1983). Stochastic simulation of high-frequency ground motions based on seismological models of the radiated spectra, *Bull. Seismol. Soc. Am.* **73**, 1865–1894.
- Boore, D. M. (2003). Simulation of ground motion using the stochastic method, *Pure Appl. Geophys.* **160**, 635–676, doi: [10.1007/PL00012553](https://doi.org/10.1007/PL00012553).
- Boore, D. M. (2016). Determining generic velocity and density models for crustal amplification calculations, with an update of the Boore and Joyner (1997) generic site amplification for, *Bull. Seismol. Soc. Am.* **106**, 313–317, doi: [10.1785/0120150229](https://doi.org/10.1785/0120150229).
- Boore, D. M., and G. M. Atkinson (2008). Ground-motion prediction equations for the average horizontal component of PGA, PGV, and 5%-damped PSA at spectral periods between 0.01 s and 10.0 s, *Earthq. Spectra* **24**, 99–138.
- Boore, D. M., J. P. Stewart, E. Seyhan, and G. M. Atkinson (2014). NGA-West2 equations for predicting PGA, PGV, and 5% damped PSA for shallow crustal earthquakes, *Earthq. Spectra* **30**, no. 3, 1057–1085, doi: [10.1193/070113EQS184M](https://doi.org/10.1193/070113EQS184M).
- Brune, J. (1971). Correction [to "Tectonic stress and the spectra, of seismic shear waves from earthquakes"], *J. Geophys. Res.* **76**, 5002, doi: [10.1029/JB076i020p05002](https://doi.org/10.1029/JB076i020p05002).
- Brune, J. N. (1970). Tectonic stress and the spectra of seismic shear waves from earthquakes, *J. Geophys. Res.* **75**, 4997–5009, doi: [10.1029/JB075i026p04997](https://doi.org/10.1029/JB075i026p04997).
- Bufoñ, E., C. López-Sánchez, L. Lozano, J. M. Martínez-Solares, S. Cesca, C. S. Oliveira, and A. Udiá (2020). Re-evaluation of seismic intensities and relocation of 1969 Saint Vincent Cape seismic sequence: A comparison with the 1755 Lisbon earthquake, *Pure Appl. Geophys.* **177**, 1781–1800, doi: [10.1007/s0024-019-02336-8](https://doi.org/10.1007/s0024-019-02336-8).
- Carrilho, F., S. Custódio, M. Bezzeghoud, C. S. Oliveira, C. Marreiros, D. Vales, P. Alves, A. Pena, G. Madureira, M. Escuer, et al. (2021). The Portuguese national seismic network—Products and services, *Seismol. Res. Lett.* **92**, 1541–1570, doi: [10.1785/0220200407](https://doi.org/10.1785/0220200407).
- Carvalho, A., G. Zonno, G. Franceschina, J. B. Serra, and A. C. Costa (2008). Earthquake shaking scenarios for the metropolitan area of Lisbon, *Soil Dynam. Earthq. Eng.* **28**, 347–364, doi: [10.1016/j.soildyn.2007.07.009](https://doi.org/10.1016/j.soildyn.2007.07.009).
- Chiou, B.-J., and R. R. Youngs (2008). An NGA model for the average horizontal component of peak ground motion and response spectra, *Earthq. Spectra* **24**, 173–215.
- Danciu, L., S. Nandan, C. G. Reyes, R. Basili, G. Weatherill, C. Beauval, A. Rovida, S. Vilanova, K. Sesetyan, P. Y. Bard, et al. (2021). The 2020 update of the European Seismic Hazard Model—ESHM20: Model Overview, *EFEHR Technical Rept. 001 v.1.0.0*, 1 pp., doi: [10.12686/a15](https://doi.org/10.12686/a15).
- Delavaud, E., F. Cotton, S. Akkar, F. Scherbaum, L. Danciu, C. Beauval, S. Drouet, J. Douglas, R. Basili, M. A. Sandikkaya, et al. (2012). Toward a ground-motion logic tree for probabilistic seismic hazard assessment in Europe, *J. Seismol.* **16**, 451–473.
- Derakhshani, A., and A. H. Foruzan (2019). Predicting the principal strong ground motion parameters: A deep learning approach, *Appl. Software Comput.* **80**, 192–201, doi: [10.1016/j.asoc.2019.03.029](https://doi.org/10.1016/j.asoc.2019.03.029).
- Derras, B., P. Y. Bard, and F. Cotton (2014). Towards fully data driven ground-motion prediction models for Europe, *Bull. Earthq. Eng.* **12**, 495–516, doi: [10.1007/s10518-013-9481-0](https://doi.org/10.1007/s10518-013-9481-0).

- Dhanya, J., and S. T. G. Raghukanth (2018). Ground motion prediction model using artificial neural network, *Pure Appl. Geophys.* **175**, 1035–1064, doi: [10.1007/s00024-017-1751-3](https://doi.org/10.1007/s00024-017-1751-3).
- Di Giacomo, D., I. Bondár, D. A. Storchak, E. R. Engdahl, P. Bormann, and J. Harris (2015). ISC-GEM: Global Instrumental Earthquake Catalogue (1900–2009), III. Re-computed MS and m_b , proxy M_w , final magnitude composition and completeness assessment, *Phys. Earth Planet. In.* **239**, 33–47, doi: [10.1016/j.pepi.2014.06.005](https://doi.org/10.1016/j.pepi.2014.06.005).
- Diaz, J., J. Gallart, and R. Carbonell (2016). Moho topography beneath the Iberian-western Mediterranean region mapped from controlled-source and natural seismicity surveys, *Tectonophysics* **692**, 74–85, doi: [10.1016/j.tecto.2016.08.023](https://doi.org/10.1016/j.tecto.2016.08.023).
- Dif, Z., B. Derras, F. Cotton, and C. Molkenthin (2020). Data-driven testing of the magnitude dependence of earthquake stress parameters using the NGA-West 2 dataset, *J. Seismol.* **24**, 1095–1107, doi: [10.1007/s10950-020-09952-1](https://doi.org/10.1007/s10950-020-09952-1).
- Douglas, J. (2022). Ground motion prediction equations 1964–2021, available at <http://www.gmpe.org.uk> (last accessed January 2024).
- Drouet, S., and F. Cotton (2015). Regional stochastic GMPEs in low-seismicity areas: Scaling and aleatory variability analysis—Application to the French Alps, *Bull. Seismol. Soc. Am.* **105**, 4, 1883–1902, doi: [10.1785/0120140240](https://doi.org/10.1785/0120140240).
- Edwards, B., and D. Fäh (2013). A stochastic ground-motion model for Switzerland, *Bull. Seismol. Soc. Am.* **103**, 78–98, doi: [10.1785/0120110331](https://doi.org/10.1785/0120110331).
- Fonseca, J., and S. P. Vilanova (2010). The 23 April 23 1909 Benavente (Portugal) M 6.3 earthquake, *Seismol. Res. Lett.* **81**, no. 3, 534–536, doi: [10.1785/gssrl.81.3.534](https://doi.org/10.1785/gssrl.81.3.534).
- Frankel, A. (2004). How can seismic hazard around the new Madrid seismic zone be similar to that in California? *Seismol. Res. Lett.* **75**, 575–586, doi: [10.1785/gssrl.75.5.575](https://doi.org/10.1785/gssrl.75.5.575).
- Haendel, A., M. Pilz, and F. Cotton (2023). Hard rock κ_0 at KiK-net sites in Japan, *Bull. Seismol. Soc. Am.* **113**, 6, 2650–2665, doi: [10.1785/0120220246](https://doi.org/10.1785/0120220246).
- Hartzell, S. H. (1978). Earthquake aftershocks as Green's functions, *Geophys. Res. Lett.* **5**, 1–4, doi: [10.1029/GL005i001p00001](https://doi.org/10.1029/GL005i001p00001).
- Haykin, S. (2009). *Neural Networks and Learning Machines*, Pearson, New Jersey.
- Joyner, W. B., and D. M. Boore (1993). Methods for regression analysis of strong-motion data, *Bull. Seismol. Soc. Am.* **83**, 469–487, doi: [10.1785/BSSA0830020469](https://doi.org/10.1785/BSSA0830020469).
- Kalakonas, P., and V. Silva (2021). Seismic vulnerability modelling of building portfolios using artificial neural networks, *Earthq. Eng. Struct. Dynam.* **51**, 310–327, doi: [10.1002/eqe.3567](https://doi.org/10.1002/eqe.3567).
- Kalakonas, P., and V. Silva (2022). Earthquake scenarios for building portfolios using artificial neural networks: Part I—Ground motion modelling, *Bull. Earthq. Eng.* doi: [10.1007/s10518-022-01598-3](https://doi.org/10.1007/s10518-022-01598-3).
- Kempton, J. J., and J. P. Stewart (2006). Prediction equations for significant duration of earthquake ground motions considering site and near-source effects, *Earthq. Spectra* **22**, no. 4, 985–1013, doi: [10.1193/1.2358175](https://doi.org/10.1193/1.2358175).
- Khosravikia, F., and P. Clayton (2021). Machine learning in ground motion prediction, *Comput. Geosci.* **148**, 104700, doi: [10.1016/j.cageo.2021.104700](https://doi.org/10.1016/j.cageo.2021.104700).
- Kingma, D. P., and J. Ba (2014). ADAM: A method for stochastic optimization, doi: [10.48550/arXiv.1412.6980](https://doi.org/10.48550/arXiv.1412.6980).
- Kotha, S. R., G. Weatherill, D. Bindi, and F. Cotton (2020). A regionally-adaptable ground-motion model for shallow crustal earthquakes in Europe, *Bull. Earthq. Eng.* **18**, 4091–4125, doi: [10.1007/s10518-020-00869-1](https://doi.org/10.1007/s10518-020-00869-1).
- Lam, N., J. Wilson, and G. Hutchinson (2000). Generation of synthetic earthquake accelerograms using seismological modelling: A review, *J. Earthq. Eng.* **4**, 321–354, doi: [10.1080/13632460009350374](https://doi.org/10.1080/13632460009350374).
- Motazedian, D., and G. M. Atkinson (2005). Stochastic finite-fault modeling based on a dynamic corner frequency, *Bull. Seismol. Soc. Am.* **95**, 995–1010, doi: [10.1785/0120030207](https://doi.org/10.1785/0120030207).
- Muggeo, V. M. R. (2003). Estimating regression models with unknown break-points, *Stat. Med.* **22**, 3055–3071, doi: [10.1002/sim.1545](https://doi.org/10.1002/sim.1545).
- Oliveira, C. S., L. A. Mendes-Victor, J. Gaspar, and G. Silveira (1988). Seismic impact of future earthquakes in the Town of Lisbon: An example of application, *Proc. of the 9th World Conf. on Earthquake Engineering*, Tokyo, Japan, 2–9 August 1988.
- Pagani, M., D. Monelli, G. Weatherill, L. Danciu, H. Crowley, V. Silva, P. Henshaw, L. Butler, M. Nastasi, L. Panzeri, et al. (2014). OpenQuake engine: An open hazard (and risk) software for the global earthquake model, *Seismol. Res. Lett.* **85**, no. 3, 692–702, doi: [10.1785/0220130087](https://doi.org/10.1785/0220130087).
- Perlovsky, L. (2001). *Neural Networks and Intellect: Using Model Based Concepts*, Oxford University Press, London, United Kingdom.
- Pezeshk, S., A. Zandieh, and B. Tavakoli (2011). Hybrid empirical ground-motion prediction equations for eastern North America using NGA models and updated seismological parameters, *Bull. Seismol. Soc. Am.* **101**, 1859–1870, doi: [10.1785/0120100144](https://doi.org/10.1785/0120100144).
- Pilgrim, C. (2021). piecewise-regression (aka segmented regression) in Python, *J. Open-Source Software* **6**, 3859, doi: [10.21105/joss.03859](https://doi.org/10.21105/joss.03859).
- Raoof, M., R. B. Herrmann, and L. Malagnini (1999). Attenuation and excitation of three-component ground motion in southern California, *Bull. Seismol. Soc. Am.* **89**, 888–902.
- Rietbrock, A., F. Strasser, and B. Edwards (2013). A stochastic earthquake ground-motion prediction model for the United Kingdom, *Bull. Seismol. Soc. Am.* **103**, 57–77, doi: [10.1785/0120110231](https://doi.org/10.1785/0120110231).
- Rodriguez-Marek, A., G. A. Montalva, F. Cotton, and F. Bonilla (2011). Analysis of single-station standard deviation using the KiK-net data, *Bull. Seismol. Soc. Am.* **101**, no. 3, 1242–1258, doi: [10.1785/0120100252](https://doi.org/10.1785/0120100252).
- Scholz, C. H., C. A. Aviles, and S. G. Wesnousky (1986). Scaling differences between large interplate and intraplate earthquakes, *Bull. Seismol. Soc. Am.* **76**, 65–70.
- Shible, H., F. Hollender, D. Bindi, P. Traversa, A. Oth, B. Edwards, P. Klin, H. Kawase, I. Grendas, R. R. Castro, et al. (2022). GITEC: A generalized inversion technique benchmark, *Bull. Seismol. Soc. Am.* **112**, no. 2, 850–877, doi: [10.1785/0120210242](https://doi.org/10.1785/0120210242).
- Sokolov, V., R. Kiuchi, W. D. Mooney, and H. M. Zahran (2021). Regional ground-motion prediction equations for western Saudi Arabia: Merging stochastic and empirical estimates, *Bull. Earthq. Eng.* **19**, 1663–1686, doi: [10.1007/s10518-021-01048-6](https://doi.org/10.1007/s10518-021-01048-6).
- Sousa, M. L., and C. S. Oliveira (1996). Hazard mapping based on macroseismic data considering the influence of geological conditions, *Nat. Hazards* **14**, 207–225, doi: [10.1007/BF00128267](https://doi.org/10.1007/BF00128267).
- Stafford, P. J. (2014). Crossed and nested mixed-effects approaches for enhanced model development and removal of the ergodic

- assumption in empirical ground-motion models, *Bull. Seismol. Soc. Am.* **104**, 702–719, doi: [10.1785/0120130145](https://doi.org/10.1785/0120130145).
- Stewart, J. P., G. A. Parker, G. M. Atkinson, D. M. Boore, Y. M. Hashash, and W. J. Silva (2020). Ergodic site amplification model for central and eastern North America, *Earthq. Spectra* **36**, 42–68, doi: [10.1177/8755293019878185](https://doi.org/10.1177/8755293019878185).
- Toro, G. R. (2002). Modification of the Toro et al. (1997) attenuation equations for large magnitudes and short distances, *Risk Engineering Technical Rept.* 10 pp.
- Toro, G. R., N. A. Abrahamson, and J. F. Schneider (1997). Model of strong ground motions from earthquakes in central and eastern North America: Best estimates and uncertainties, *Seismol. Res. Lett.* **68**, 41–57, doi: [10.1785/gssrl.68.1.41](https://doi.org/10.1785/gssrl.68.1.41).
- Trugman, D. T. (2020). Stress-drop and source scaling of the 2019 Ridgecrest, California, earthquake sequence, *Bull. Seismol. Soc. Am.* **110**, no. 4, 1859–1871, doi: [10.1785/0120200009](https://doi.org/10.1785/0120200009).
- Vales, D., J. Havskov, L. Matias, and S. Silva (2020). Evidence of high lateral variations of coda Q from local earthquakes in western Iberia and its SW offshore area, *Tectonophysics* **791**, 228564, doi: [10.1016/j.tecto.2020.228564](https://doi.org/10.1016/j.tecto.2020.228564).
- Van Houtte, C., S. Drouet, and F. Cotton (2011). Analysis of the origins of (Kappa) to compute hard rock to rock adjustment factors for GMPEs, *Bull. Seismol. Soc. Am.* **101**, 2926–2941, doi: [10.1785/0120100345](https://doi.org/10.1785/0120100345).
- Vilanova, S. P., and J. F. B. D. Fonseca (2007). Probabilistic seismic-hazard assessment for Portugal, *Bull. Seismol. Soc. Am.* **97**, 1702–1717, doi: [10.1785/0120050198](https://doi.org/10.1785/0120050198).
- Vilanova, S. P., J. F. B. D. Fonseca, and C. S. Oliveira (2012). Ground-motion models for seismic-hazard assessment in western Iberia: Constraints from instrumental data and intensity observations, *Bull. Seismol. Soc. Am.* **102**, 169–184, doi: [10.1785/0120110097](https://doi.org/10.1785/0120110097).
- Weatherill, G., H. Crowley, A. Rouillé, B. Tourrière, A. Lemoine, C. Gracianne, S. R. Kotha, and F. Cotton (2022). Modelling site response at regional scale for the 2020 European Seismic Risk Model (ESRM20), *Bull. Earthq. Eng.* doi: [10.1007/s10518-022-01526-5](https://doi.org/10.1007/s10518-022-01526-5).
- Wells, D. L., and K. J. Coppersmith (1994). New empirical relationships among magnitude, rupture length, rupture width, rupture area, and surface displacement, *Bull. Seismol. Soc. Am.* **84**, no. 4, 974–1002, doi: [10.1785/BSSA0840040974](https://doi.org/10.1785/BSSA0840040974).
- Wilkie, J., and G. Gibson (1995). Estimation of seismic quality factor Q for Victoria, Australia, Geoscience Australia, Australia.
- Woessner, J., D. Laurentiu, D. Giardini, H. Crowley, F. Cotton, G. Grünthal, G. Valensise, R. Arvidsson, R. Basili, M. B. Demircioglu, et al. (2015). The 2013 European Seismic Hazard Model: Key components and results, *Bull. Earthq. Eng.* **13**, 3553–3596, doi: [10.1007/s10518-015-9795-1](https://doi.org/10.1007/s10518-015-9795-1).
- Xie, Y., M. Sichani Ebad, J. E. Padgett, and R. DesRoches (2020). The promise of implementing machine learning in earthquake engineering: A state-of-the-art review, *Earthq. Spectra* **36**, 1769–1801, doi: [10.1177/8755293020919419](https://doi.org/10.1177/8755293020919419).
- Xu, B., E. M. Rathje, Y. Hashash, J. Stewart, K. Campbell, and W. J. Silva (2020). κ_0 for soil sites: Observations from KiK-net sites and their use in constraining small-strain damping profiles for site response analysis, *Earthq. Spectra* **36**, no. 1, 111–137, doi: [10.1177/8755293019878188](https://doi.org/10.1177/8755293019878188).
- Zafarani, H., L. Luzi, G. Lanzano, and M. R. Soghrat (2018). Empirical equations for the prediction of PGA and pseudo spectral accelerations using Iranian strong-motion data, *J. Seismol.* **22**, 263–285.

Manuscript received 6 October 2023

Published online 11 July 2024